Electromagnetic calculations for multiscale and multiphysics simulations: a new perspective

Dung N. Pham,[1,2,a)] Sathwik Bharadwaj,[1,2,b)] and L. R. Ram-Mohan[1,2,3,4,c)]
[1)]*Department of Physics, Worcester Polytechnic Institute, Worcester, MA 01609, USA.*
[2)]*Center for Computational NanoScience, Worcester Polytechnic Institute, Worcester, MA 01609, USA.*
[3)]*Department of Electrical and Computer Engineering, Worcester Polytechnic Institute, Worcester, MA 01609, USA.*
[4)]*Department of Mechanical Engineering, Worcester Polytechnic Institute, Worcester, MA 01609, USA.*

Present day electromagnetic field calculations have basic limitations since they employ techniques based on edge-based discretization methods. While these vector finite element methods (VFEM) solve the issues of tangential continuity of fields and the removal of spurious solutions, the resulting fields do not have a unique directionality at nodes in the discretization mesh. This review presents three calculations of electromagnetic fields: (*i*) waveguides, (*ii*) cavity fields, and (*iii*) photonic crystals. We have developed Hermite interpolation polynomials and node-based finite element methods in the framework of variational principles. We show that the Hermite-finite element method (HFEM) better accuracy with lower computational cost, and provides field directional continuity across the discretized space. It also permits multiscale calculations with mixed physics. For example, the nanoscale modeling of quantum well semiconductor laser structures has to be done together with cavity electrodynamics at the micron scale in vertical-cavity surface emitting lasers and other optoelectronic systems. These can be treated with high accuracy with the new HFEM, which is also applicable to quantum mechanical simulations in meso- and nano-scale systems. We use group representation theory to derive the HFEM polynomial basis set in two dimensions. In three dimensions we derive these polynomials using usual methods. We show that degeneracies in the frequency spectrum in a cubic cavity can be denumerably large even though the symmetry of the cube, O_h, supports only singlets, doublets, or triplets. The additional operators available for the problem explains the origin of this "accidental degeneracy." We discuss this remarkable degeneracy and its reduction in detail. We consider photonic crystals corresponding to a 2D checkerboard superlattice structure, and the Escher drawing of "The Horsemen" which satisfies the nonsymmorphic group *pg*. We show that HFEM is able to deliver high accuracy in such spatially complex examples with far less computational effort than Fourier expansion methods. Finite element analysis employs geometric discretization and hence transcends geometrical limitations. Techniques explained here can be immediately extended to realistic and geometrically complex structures. The new algorithms developed here hold the promise of successful modeling of multi-physics systems. This general method is applicable to a broad class of physical systems, e.g., to semiconducting lasers which require simultaneous modeling of transitions in quantum wells or dots together with EM cavity calculations, to modeling plasmonic structures in the presence of EM field emissions, and to on-chip propagation within monolithic integrated circuits.

PACS numbers: 84.40.Az, 03.50.De, 41.20.-q, 43.20.Mv, 42.82.Et, 41.20.Jb, 84.40.-x, 02.70.Dh, 42.55.Tv, 78.67.Pt
Keywords: cavity resonators, photonic crystals, waveguides, multiscale modeling, Hermite interpolation polynomials, finite element method, accidental degeneracy

1 February 2022

CONTENTS

[a)]Electronic mail: dnpham@wpi.edu
[b)]Electronic mail: sathwik@wpi.edu
[c)]Electronic mail: lrram@wpi.edu

I. INTRODUCTION

The idea of guiding electromagnetic waves along conducting rods has been of interest for more than a century.[1] During the 1940s, the need to design radars for detection of aircraft and warships provided a new impetus for the analysis of waveguides. Schwinger[2,3] was responsible for the theoretical framework for designing waveguides with complex shapes and embedded dielectrics. With the advent of digital computation in the past 60 years, it became possible to consider problems with waveguide geometries and characteristics that had no closed-form analytical solutions. In particular, the numerical simulation of the behavior of electromagnetic waves at the microwave frequencies attracted much interest from their use in transmitters and receivers of radio waves. High-accuracy calculations of electromagnetic fields through geometry discretization has been the focus of intense investigation over this period. The approach offers detailed real-space information appropriate for the analysis of fields not only in open domains but in closed regions of complicated structure, such as the dielectric, magnetic and semiconducting layers encountered in radio frequency integrated circuits. The impact of predictive capability with this approach in electromagnetic simulation has been profound for problems ranging from antenna design to on-chip signal propagation. Typically, the on-chip electromagnetic solvers are invoked for modeling ports and guiding structures, the device solvers are parameterized models, and the passives are lumped elements. While this design philosophy has been very successful at lower frequencies and for large devices, the eventual addition of full-wave electromagnetic solvers to fully integrated chip layout and device design modeling tools is a foregone conclusion.

This leads to the critical issue of obtaining field calculations that provide the spatial resolution adequate for multiscale problems, for example, field propagation into and out of active electronic devices that are much smaller than the wavelengths of the propagating signals they manipulate. For RF circuits operating at sub-millimeter wave frequencies, the designs of transitions and interactions of signals at the transistor level are intensive engineering exercises to obtain the critical matching conditions that make useful circuits possible at these demanding frequencies.[4] Given the geometric complexities and the material loss components that are relevant with increasing frequency above 300 GHz, most design cycles require extensive back-fitting to measurement and redesign. This iterative process is very expensive in time and fabrication costs compared with design methods at lower frequencies where the full-wave modeling can be restricted to port transitions and guiding structures of minimal loss. Therefore, a solver methodology that can obtain high spatial resolution without poor computational scaling and discretization error behaviors is a key element of integrating full-wave electromagnetics when small (10's of nanometers) active devices interact with metals and dielectrics that are far from perfect conductors or lossless. Figure 1 shows a schematic of a vertical cavity surface emitting laser (VCSEL) as an example of a multiscale application in which the active quantum well region is of nanometer scale while the photonic cavity is at the micron scale.

In this review, we also consider cavity electrodynamics, level degeneracies in a cubic cavity, and their identification. We show that the electrodynamic cubic cavity exhibits "accidental degeneracy." We explore the dynamic interaction between symmetry, level degeneracy, and its removal.

Finally, we demonstrate the efficacy of HFEM in the modeling of photonic crystals (PC). We consider a checkerboard superlattice wires and a beautiful application to Escher's drawing, "The Horsemen," treated as a photonic crystal having a nonsymmorphic symmetry group *pg*.

II. EARLIER APPROACHES

The Vector finite element method

The most favorable trade-off from a numerical standpoint has been to sacrifice polynomial degrees of freedom for the representation of either the normal or tangential fields in exchange for compliance with Nedelec conditions. The mainstay of this approach is the use of Nedelec-compliant vector finite elements (VFEM).[5–10] The most widely implemented element basis functions share a common attribute that tangential field boundary conditions are explicit at triangle boundaries and that normal field representations are one polynomial order

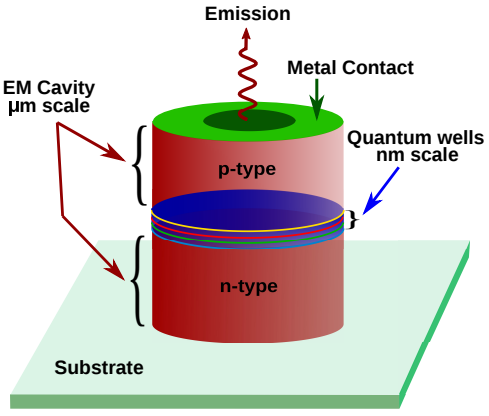

FIG. 1: A schematic of a vertical cavity surface emitting laser (VCSEL) is shown. The quantum well is sandwiched two semiconducting cylinders. The quantum well region has the geometry at the nanometer scale, while the photonic cavity is at the micron scale.

less than that of the tangential fields. These conditions and the mixed-order field representations are well-documented and effort has been made to suppress potentially unphysical solutions through the VFEM basis choices.[9]

The disadvantage of mixed-order polynomial approaches is the inherent imbalance in discretization error with increasing mesh density. While every discretization method introduces errors with arbitrary mesh scaling, *h*-convergence is achieved in a well behaved finite element calculation, and it would be expected that increasing mesh density where solutions change rapidly should provide much better real space functions until extremely dense conditions prevail. However, in mixed order elements, mesh refinement toward a dense grid of equilateral triangles (in 2D) can decrease the overall quality of the field representation in polynomials because increasing portions of real space are described by lower order polynomials since field components with projections normal to the triangle boundaries occur ubiquitously.

In the limit of a very dense mesh, the entire solution can be no better than the lowest order description because the inter-element boundary regions dominate over the vanishing triangle interior. What is worse is that the as-written basis functions produce ambiguous vector fields at triangle vertices in the sense that approaching a point in space that is shared as a common corner node of several triangles produces fields that are unique to each triangle, creating an overdetermined basis representation for the fields at vertices. (See Fig. 2.) This occurs because the basis decomposes the field there as projections orthogonal to adjacent edges that are not shared among all the triangles sharing the node. Therefore, an extremely dense mesh results in at best a constant value description if additional numerical techniques are not deployed to mitigate the problem of multiple definitions of the vector field at shared vertices. In addition, when such fields calculated using VFEM are employed in further applications, such as determining electron trajectories in accelerators or in high power vacuum tube design, these regions around vertices inject uncertainties in the charged particle trajectories.

Given the inherent side effects of vector basis element discretization, it is not surprising that most of the work on VFEM solution enhancement and refinement has focused on the construction of higher order polynomial basis functions to increase spatial resolution rather than dense meshing (*p*-convergence). Hierarchical approaches are used in practice and have been published in great detail.[11,12] In practice, the difficulty with this route to better spatial resolution is that mesh refinement or the discretization of disparately sized physical regions often requires the mating of finite elements with different basis orders.

The enormous advantages to finding a nodal basis that scales well with meshing refinement make this an attractive topic to re-engage. The spectral pollution that arises from nodal based basis functions has been analyzed elegantly from a mathematical point of view for traditional choices of polynomials.[13]

The present article analyzes, for comparable degrees of freedom (DOF), the impact of choosing an alternative nodal basis formed from Hermite interpolation polynomials *versus*

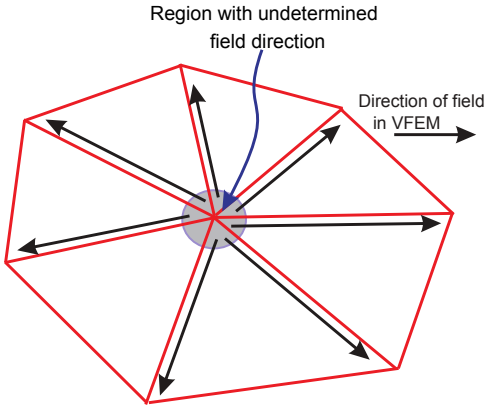

FIG. 2: We show the vector fields at vertices in the edge-elements in VFEM. These are directed along the edges, leading to a region of ill-defined direction for the field at each vertex. Thus the more the number of vertices the larger is the region of poorly defined fields.

the use of vector finite elements. The advantages of the Hermite finite element method (HFEM) are shown for canonical waveguide problems and compared to published treatments. The nodal representation with function and derivative continuity (the core of the Hermite approach) results in unambiguous field descriptions at shared nodes among triangles and treats the field components with uniform polynomial degree (not mixed-order.) The built-in access to derivative quantities should offer ready access to quantities that are useful for sensitivity analysis.[14] This treatment results in global functions without severe coarsening which will be suitable for analyzing interactions with small features, such as those found in high frequency transistor circuits. In an on-chip calculation, including transitions to coplanar waveguide and micro-strip waveguide structures, some thin film layers will set a mesh size that is incompatible with the overall structure size and propagating signal wavelength. At present, these treatments in circuit design software are dominated by finite-difference time-domain methods.[15]

The boundary element method

For external regions, boundary integral techniques have been combined with finite element methods to capture the asymptotic behavior in open systems.[16] While offering surface vs. volume discretization advantages, boundary integral formulations are self-consistency relations and do not enjoy the advantages of variational quadratic convergence. The use of dyadic Green's functions in EM involves derivatives of these singular functions at the boundaries making the evaluation of the integrals more complex. Dimensional continuation techniques applied for the evaluation of such hypersingular integrals will substantially enhance the computational accuracy.[17] However, the matrices generated in this method are dense, and are typically nonlinear in the eigenfrequencies.

Other methods

Finally, meshless methods[18–20] have been used to treat a number of physics problems, including EM, and are at the

opposite extreme in terms of numerical representations to the method given in this paper where we develop a higher order of derivative continuity in spatial basis. Meshless schemes can be interpreted in many ways, but often involve the use of basis functions that are not restricted to a finite volume. The resulting matrix formulations have the advantage of being fully block-diagonal but require a separate treatment of continuity boundary conditions. In these situations the boundary conditions are enforced as a constraint which can be a penalty method or numerical flux minimization. Derivative information is rarely treated when forming eigenfunctions in these methods.

III. THE SOURCE OF SPURIOUS SOLUTIONS

EM fields in a physical system should satisfy the wave equation along with a divergence-free condition. For example, in the electric field formulation (E-field), we solve Maxwell's equations

$$\nabla \times \nabla \times \mathbf{E} = \varepsilon \mu \omega^2 \mathbf{E}; \tag{1}$$

$$\nabla \cdot \varepsilon \mathbf{E} = 0, \tag{2}$$

where ω is the eigenfrequency and ε and μ are the permittivity and permeability of the material. Computationally if we simply attempt to solve the wave equation Eq. (1), we are not guaranteed that the obtained solutions satisfy the divergence-free condition of Eq. (2). Solutions with either zero frequency ($\omega = 0$) or with non-zero divergence ($\nabla \cdot \varepsilon \mathbf{E} \neq 0$) that are obtained while solving Eq. (1) are known as the spurious (unphysical) solutions. Such spurious solutions also corrupt the desired eigenspectrum.

The vector basis functions can be constructed in VFEM to systematically eliminate spurious solutions by casting them into the null space of the curl operator.[6,9,21] These solutions correspond to the zero-frequency (static) solutions in the EM problems. For matrix dimensions of 10^3 in typical EM calculations, nearly 20-30% of the solutions belong to this class and are thrown away, being unusable solutions.[9] Carrying this overhead in the calculation is computationally expensive when scaling to sophisticated structures.

In large scale computations where the method of domain decomposition is often employed, all solutions for each sub-domain are calculated so that the solutions for the entire domain can be constructed from those of the sub-domains. The zero-frequency modes of a sub-domain are also needed as Fourier components in order to construct the global solutions. However, it is not simple to discriminate between acceptable zero frequency solutions and the pollution of the nullspace with spurious solutions.

IV. THE PROPOSED HERMITE FINITE ELEMENT METHOD

We propose the use of the Hermite basis functions because they employ spatial derivative degrees of freedom that directly coincide with the operators in the curl, and are completely consistent with EM theory. We show that the approach yields better accuracy, with a more physical (smoother) representation of fields, than from VFEM. In 2D calculations, this method does not generate the spurious solutions that plagued nodal based Lagrange FEM encountered earlier in the 1970's, even though the C_1-continuous Hermite polynomials are also scalar in nature. Our alternative set of polynomial basis functions for 2D, the scalar fifth-order Hermite interpolation polynomials for the numerical calculations of EM fields removes all the above difficulties. These polynomials are associated with degrees of freedom that include both function value and spatial derivatives up to second order. Recently, Kassebaum, Boucher and Ram-Mohan (KBR)[22] have shown how to derive these polynomials using group representation theory, giving a comparison with the earlier basis functions occurring in the literature,[23–27] which use the same derivative degrees of freedom but are distinct from existing sets of polynomials.

In our approach, each in-plane component of the field is represented by scalar Hermite shape functions. The method is equally effective with E-fields and H-fields, as we will demonstrate. These functions ensure tangential continuity along shared sides of triangles, thereby eliminating spurious solutions. The C_1-continuity perpendicular to the sides of the triangular elements leads to smoother reconstruction of solutions. This representation guarantees consistency in the field direction at the vertices of triangles. These properties allow for more accurate solutions of electrodynamics problems with faster h-convergence because of the higher derivative shape functions. We show here that the scalar HFEM yields four orders of magnitude higher accuracy with fewer elements than those needed in the presently prevalent methods for waveguides.[28]

In two dimensional (2D) waveguides, we circumvent the issue of spurious solutions by solving for only one of the field components (H_z or E_z), and obtain the other two components using boundary conditions (BCs) and the divergence-free condition.[29–31] However, such freedom does not exist in three dimensions (3D). In a numerical calculation, the anticipated zero frequency solutions can have non-zero frequencies due to discretization, and will occur inter-mixed with the physical spectrum.[9,32]

Nodal representation of field components with scalar functions and their derivatives results in an unambiguous field description at shared nodes among adjacent elements and treats the field components on a uniform footing.[33] The built-in derivative degrees of freedom (DOFs) allow us to readily calculate the additional quantities such as surface currents, while providing smoother solutions. This treatment results in global functions without severe coarsening which will be suitable for analyzing interactions with small features, such as those found in high frequency transistor circuits and VCSELs. Within this scheme, dielectric discontinuities along interfaces can be handled cleanly using Fermi smoothing functions.[34]

For the brick element in 3D, the polynomials are constructed from the outer product of the 1D Hermite polynomials.[27] For a tetrahedral element, the Hermite polynomials are generated directly based on the geometry of the

tetrahedron and conditions on function values and derivatives at the vertex nodes and mid-face nodes. *We then have for both types of element polynomials with both tangential and normal derivative continuity across the element boundary.* We note that the HFEM approach yields better accuracy, with a smoother representation of fields than those obtained using VFEM. The HFEM scheme yields several orders of higher accuracy with fewer elements than those needed in the presently prevalent 3D implementations of VFEM.[35–37] The node-based HFEM representation guarantees consistency in the direction of fields at the vertices of elements.[38] We impose the divergence-free condition through a constant Lagrange multiplier term introduced into the action integral in 3D, and also by explicitly requiring a zero-divergence condition at each node through the derivative DOFs available at each node in our formulation. Any surviving $\omega \neq 0$ spurious solutions are then eliminated by identifying them using their large $|\nabla \cdot \mathbf{E}|/|\nabla \times \mathbf{E}|$ ratio. We demonstrate that this procedure does not alter or influence the accuracy of the physical solutions.

In VFEM implementations, the eigenfrequencies of spurious solutions are pushed to zero, either through the Nedelec conditions or through their removal at each iteration, as mentioned earlier. In either case, this is an expensive numerical procedure. In the literature, the first approach for eliminating spurious solutions with scalar polynomials was the penalty factor method (*i. e.*, a Lagrange multiplier scheme).[39] However, a fixed choice of the penalty factor fails to impose the zero-divergence condition adequately for all frequencies.[21] Furthermore, the penalty term itself can introduce an additional set of spurious solutions.[40]

Within the HFEM framework for 3D calculations, we now have the luxury of explicitly imposing a zero-divergence condition at each node while using Hermite interpolation polynomials since we have derivative degrees of freedom there.[41–43] While this does not ensure the complete removal of the divergence in the interior of the finite element through interpolation, it reduces it substantially, especially as the size of the element is reduced. In this article, we use a constant penalty factor, and impose zero-divergence at all nodes to identify the spurious solutions for elimination. Either brick elements (216 DOFs) or tetrahedral elements (56 DOFs) can be used in the calculations.

The full spectrum of propagating modes in a partially filled rectangular waveguide is obtained with HFEM and compared with analytic solutions. We plot the eigenfrequencies of the different modes which shows the existence of cut-offs in the propagating mode frequencies which agree perfectly with the analytic solutions. The magnetic fields for various modes are plotted to show the continuous character of the solutions in HFEM. The capturing of eigenstates in the higher dielectric region as dielectric contrast increases is analogous to the evolution of the electronic states in an asymmetric quantum well from above-barrier states to states bound in the quantum well as the barrier energy in the well region is lowered.

In the following sections we consider cavity electrodynamics within a finite element framework using Hermite brick elements and also employ tetrahedral elements for comparison.

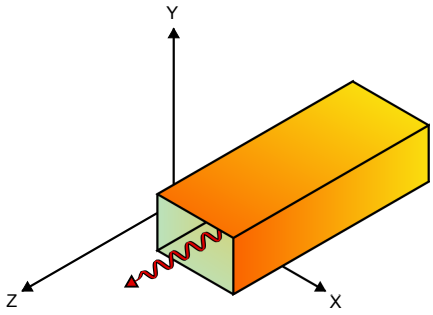

FIG. 3: A homogeneous waveguide with a rectangular cross-section $a \times b$ is shown. The propagating wave moves along the z-axis.

Finally, we show the advantages of HFEM to determine dispersion relation in photonic crystals. The lattice of dielectric cylinders is first treated in order to benchmark the method we are proposing. The application to a checkerboard superlattice is to show how dielectric corners are treated. The modeling of the Escher drawing as a final example illustrates the advantage of HFEM when the spatial complexity of the distribution of dielectric is so high that the plane wave methods are not as appropriate.

V. HFEM FORMULATION OF ELECTROMAGNETIC FIELDS

We begin with Maxwell's equations expressed in MKS units,

$$\nabla \cdot \mathbf{D} = \rho, \tag{3}$$

$$\nabla \times \mathbf{H} - \frac{\partial \mathbf{D}}{\partial t} = \mathbf{J}, \tag{4}$$

$$\nabla \times \mathbf{E} + \frac{\partial \mathbf{B}}{\partial t} = 0, \tag{5}$$

$$\nabla \cdot \mathbf{B} = 0. \tag{6}$$

In the above, the displacement vector $\mathbf{D}$ and the magnetic flux density $\mathbf{B}$ are expressed in terms of the electric and magnetic fields $\mathbf{E}$ and $\mathbf{H}$,

$$\mathbf{D} = \varepsilon \mathbf{E}; \qquad \mathbf{B} = \mu \mathbf{H}. \tag{7}$$

If the medium is isotropic, ε and μ are scalar quantities, rather than second-rank tensors. Let us define the dimensionless quantities ε_r and μ_r so that

$$\varepsilon = \varepsilon_r \varepsilon_0, \qquad \mu = \mu_r \mu_0, \tag{8}$$

with ε_0 and μ_0 being the permittivity and permeability of free space, respectively.

We assume that the dielectric regions of the waveguide are charge-free and current-free.

The Maxwell's equations are combined to form the wave

equations for the E-field and H-field,

$$\nabla\times\left(\frac{1}{\varepsilon_r}\nabla\times\mathbf{H}\right)-k_0^2\mu_r\mathbf{H}=0, \tag{9}$$

$$\nabla\times\left(\frac{1}{\mu_r}\nabla\times\mathbf{E}\right)-k_0^2\varepsilon_r\mathbf{E}=0, \tag{10}$$

where $k_0=\omega/c$. We observe that either equation may be used to set up the action integral. In order to define the action, we begin by multiplying the differential equation, Eq. (9), by $\delta\mathbf{H}^*$ and integrating over the physical domain. We use the vector identity

$$\begin{aligned}\nabla\cdot(\mathbf{P}\times\mathbf{R})&=\left[\varepsilon_{ijk}\left(\partial_i P_j\right)R_k-P_j\varepsilon_{jik}\partial_i R_k\right]\\&=(\nabla\times\mathbf{P})\cdot\mathbf{R}-\mathbf{P}\cdot(\nabla\times\mathbf{R}).\end{aligned} \tag{11}$$

Now let $\mathbf{R}=\alpha\nabla\times\mathbf{Q}$. Then from Eq. (11),

$$\begin{aligned}\nabla\cdot(\mathbf{P}\times(\alpha\nabla\times\mathbf{Q}))=&(\nabla\times\mathbf{P})\cdot(\alpha\nabla\times\mathbf{Q})\\&-\mathbf{P}\cdot(\nabla\times(\alpha\nabla\times\mathbf{Q})).\end{aligned} \tag{12}$$

This relation, along with Gauss's theorem and the substitutions $\mathbf{Q}=\mathbf{H}$, $\mathbf{P}=\delta\mathbf{H}^*$, and $\alpha=\varepsilon_r^{-1}$, leads to the integrals

$$\begin{aligned}\int_V d^3r\,\delta\mathbf{H}^*\cdot[\nabla\times\frac{1}{\varepsilon_r}(\nabla\times\mathbf{H})]=&\int_V d^3r\,(\nabla\times\delta\mathbf{H}^*)\cdot\frac{1}{\varepsilon_r}(\nabla\times\mathbf{H})\\&-\oint_S ds\,\hat{\mathbf{n}}\cdot\left[\delta\mathbf{H}^*\times\frac{1}{\varepsilon_r}(\nabla\times\mathbf{H})\right].\end{aligned} \tag{13}$$

The integrand of the surface term may be rewritten as

$$\hat{\mathbf{n}}\cdot\left[\delta\mathbf{H}^*\times\frac{1}{\varepsilon_r}(\nabla\times\mathbf{H})\right]=-\delta\mathbf{H}^*\cdot\left[\hat{\mathbf{n}}\times\frac{1}{\varepsilon_r}(\nabla\times\mathbf{H})\right]. \tag{14}$$

We are interested in solving for time-harmonic fields, so that $\mathbf{H}(\mathbf{r},t)=\mathbf{H}(\mathbf{r})\exp(-i\omega t)$ and similarly for $\mathbf{E}$. For time-harmonic fields, the relations between $\mathbf{E}$ and $\mathbf{H}$ is given by

$$\mathbf{H}=-\frac{i}{\mu\omega}\nabla\times\mathbf{E},\qquad\mathbf{E}=\frac{i}{\varepsilon\omega}\nabla\times\mathbf{H}. \tag{15}$$

Therefore, $\mathbf{E}$ is proportional to $\varepsilon_r^{-1}(\nabla\times\mathbf{H})$. Assuming the waveguide to be enclosed by a perfectly conducting material, one of the boundary conditions is that $\hat{\mathbf{n}}\times\mathbf{E}=0$. Thus, the surface integral in Eq. (13) is exactly zero.

Note that it is possible to work instead with the electric field formulation of Eq. (10). In this case, the surface term takes the form

$$\oint_S ds\,\hat{\mathbf{n}}\cdot\left[\delta\mathbf{E}^*\times\frac{1}{\mu_r}(\nabla\times\mathbf{E})\right]. \tag{16}$$

We see that for the perfectly conducting boundary, the surface term arising from an integration by parts vanishes.

We thus see that the integrated form of Eq. (9) is expressible as

$$\delta\int_V d^3r\,\frac{1}{2}\left[(\nabla\times\mathbf{H}^*)\cdot\frac{1}{\varepsilon_r}(\nabla\times\mathbf{H})-k_0^2\mu_r\mathbf{H}^*\cdot\mathbf{H}\right]=0. \tag{17}$$

Equation (17) is now interpreted as the functional variation of the action integral. (Usually the action is the time integral of the Lagrangian. Here the Lagrangian is independent of time since a harmonic solution in time is assumed. Hence the $\mathscr{A}/T$ is appropriate). We may write it as

$$\delta\mathscr{A}/T=\mathbf{L}=0. \tag{18}$$

The principle of stationary action then identifies the action to be

$$\mathbf{L}=\frac{1}{2}\int_V d^3r\left[(\nabla\times\mathbf{H}^*)\cdot\frac{1}{\varepsilon_r}(\nabla\times\mathbf{H})-k_0^2\mu_r\mathbf{H}^*\cdot\mathbf{H}\right]. \tag{19}$$

Similarly, using the electric field formulation of Maxwell's equations yields

$$\mathbf{L}=\frac{1}{2}\int_V d^3r\left[(\nabla\times\mathbf{E}^*)\cdot\frac{1}{\mu_r}(\nabla\times\mathbf{E})-k_0^2\varepsilon_r\mathbf{E}^*\cdot\mathbf{E}\right]. \tag{20}$$

In the FEM framework, the action integral is discretized into triangular elements in 2D, and either hexahedral or tetrahedral elements in 3D. For tetrahedral elements in 2D, the Hermite elements exhibit C_1 continuity throughout the finite element mesh. For a given Cartesian component of $\mathbf{H}$, say $f(x,y)$, the interpolated value in terms of the 2D Hermite basis functions ϕ_i is given by

$$f(x,y)=\sum_{i=1}^{18}f_i\phi_i(x,y), \tag{21}$$

where the f_i are degrees of freedom assigned to the function value and its derivatives at the vertices of the triangle. This allows the enforcement of either derivative continuity or EM boundary conditions depending upon the material composition of adjacent triangles. We have provided the basis for an equilateral triangle because that is the optimization goal of most mesh refinement and it is also the rationale for the KBR group theoretical development of the basis. The basis functions ϕ_i for a reference triangle and the numbering sequence for the assignment of function and derivative values at the nodes have been published elsewhere.[22,33] In Fig. 4, we plot the KBR basis polynomials, and we observe that they satisfy triangular C_{3V} symmetry.

For a hexahedral element in 3D calculations, the HFEM polynomials are constructed through the products of 1D Hermite polynomials in x,y, and z directions. This guarantees continuity of the field values f, first derivatives $\partial_x f,\partial_y f,\partial_z f$, cross-term second derivatives $\partial^2_{xy}f,\partial^2_{yz}f,\partial^2_{xz}f$, and $\partial^3_{xyz}f$. One can also employ HFEM using tetrahedral elements instead, as in many cases tetrahedra offer more flexibility in discretizing the geometry of the problem. The quintic Hermite interpolation polynomials for tetrahedral elements assures continuity for the function value f, the first derivatives $\partial_x f,\partial_y f,\partial_z f$, and all the second derivatives $\partial^2_{xx}f,\partial^2_{yy}f,\partial^2_{zz}f,\partial^2_{xy}f,\partial^2_{yz}f,\partial^2_{xz}f$, at each vertex of the tetrahedral element. At the face centers of the tetrahedron, continuity in the function value and the first derivatives are guaranteed.

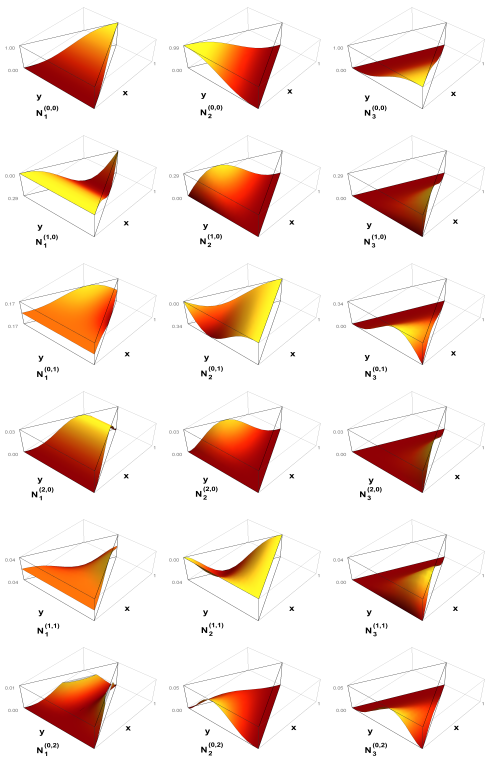

FIG. 4: The C_1-continuous 18 DOF quintic Hermite interpolation polynomials that have tangential and normal derivative continuity across the element are plotted on an equilateral triangle. These polynomials were first derived using group representation theory by KBR.[22] The superscripts on the shape function $N_i^{(m,n)}$ denote the order of the x or y derivative value set to unity at its associated node i.

VI. WAVEGUIDES

A. Boundary conditions

In this section, we consider a rectangular conducting waveguide with sides parallel to the x- and y-axes (see Fig. 3). The boundary conditions are given by

$$\hat{\mathbf{n}} \cdot \mathbf{H} = 0, \tag{22}$$
$$\hat{\mathbf{n}} \times \mathbf{E} = 0. \tag{23}$$

Expanding Eq. (22) we have

$$n_x H_x + n_y H_y = 0. \tag{24}$$

For the left and right boundaries, which are parallel to the y-axis, Eq. (24) simplifies to

$$H_x = 0 \text{ for } x \in \{0, d\}. \tag{25}$$

For the top and bottom boundaries, we get

$$H_y = 0 \text{ for } y \in \{0, h\}. \tag{26}$$

In addition, Eq. (23) may be used to generate derivative boundary conditions at the edges. Recall that the differential form of the Maxwell-Ampère equation is given by

$$\nabla \times \mathbf{H} - \frac{\partial \mathbf{D}}{\partial t} = \mathbf{J}. \tag{4}$$

Assuming that dielectric properties do not vary over time and there is no current density at the boundary, we have

$$\nabla \times \mathbf{H} = \varepsilon \frac{\partial \mathbf{E}}{\partial t} = -i\omega\varepsilon \mathbf{E} \tag{27}$$

for a time-harmonic field. Substituting Eq. (27) into Eq. (23) yields

$$\hat{n} \times \left(-\frac{1}{i\omega\varepsilon} \nabla \times \mathbf{H} \right) = 0. \tag{28}$$

Expand the cross product to obtain

$$\begin{pmatrix} n_y \left(\partial_x H_y - \partial_y H_x \right) \\ -n_x \left(\partial_x H_y - \partial_y H_x \right) \\ n_x \left(\partial_z H_x - \partial_x H_z \right) - n_y \left(\partial_y H_z - \partial_z H_y \right) \end{pmatrix} = \begin{pmatrix} 0 \\ 0 \\ 0 \end{pmatrix}. \tag{29}$$

The first and second vector components of the cross product each yield

$$\partial_x H_y = \partial_y H_x. \tag{30}$$

On the left and right boundaries, we have already shown that $H_x = 0$. Since these edges are parallel to the y-axis and $H_x = 0$ along these edges, it follows that $\partial_y H_x = 0$. From Eq. (30) we then obtain derivative conditions on H_y and H_x:

$$\partial_x H_y = 0, \text{ for } x \in \{0, d\}. \tag{31}$$
$$\partial_y H_x = 0, \text{ for } y \in \{0, h\}. \tag{32}$$

Together, Eqs. (25), (26),(31) and (32) constitute all the boundary conditions for a conducting waveguide of width d and height h.

It is straightforward to show that in 2D the divergence condition $\nabla \cdot \mathbf{E} = 0$ is automatically satisfied in calculations for the fields in the cross-section of the waveguide. We refer the reader to Nayfeh's treatment.[44]

B. Results for a homogeneous waveguide

Our first example is a homogeneous rectangular ($d \times h$) waveguide with $\varepsilon_r = 1, \mu_r = 1$, and $k_z = 1$. The dimensions of the cross-section were chosen to be $d = 20$ and $h = 10$. There is no inherent separation of TE and TM modes in the HFEM formulation and therefore the eigenproblem returns all physical solutions. The resulting H_z field components were calculated in post-processing where those with finite magnitudes are TE modes and those with H_z approaching the numerical noise floor are TM modes. The eigenfunctions for the degenerate TE and TM modes of the homogeneous waveguide

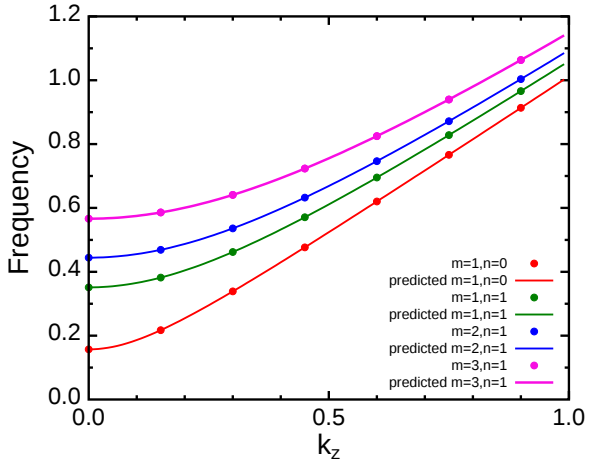

FIG. 5: Frequency eigenvalues (ω/c) of several TE$_{mn}$ modes of a hollow $(\varepsilon_r = 1)$ rectangular waveguide with 2:1 aspect ratio are shown as functions of k_z. The analytical values (curves) are compared with those calculated using HFEM (dots), and the two are essentially identical (see Table I). (From Boucher *et al.*, Ref. 33.)

were separated in post-processing since arbitrary linear combinations of degenerate modes result from a typical numerical diagonalization.

To generate pure TE modes during the postprocessing stage, we enforce the condition that

$$\frac{\partial H_y}{\partial x} - \frac{\partial H_x}{\partial y} = 0. \tag{33}$$

Since the electric field is derived from the curl of the magnetic field, this expression forces the z-component of the electric field to equal zero, creating a pure TE mode.

To create a pure TM mode, we recall that H_z is obtained from the in-plane components using the divergence condition. We can force H_z to equal zero by forcing

$$\frac{\partial H_x}{\partial x} + \frac{\partial H_y}{\partial y} = 0. \tag{34}$$

Either Eq. (33) or Eq. (34) may be enforced after calculating the eigenfunctions by multiplying one of the in-plane components, either H_x or H_y, by a scale factor until one of the equations is satisfied.

The eigenvalues of a few propagating modes are plotted as a function of k_z in Fig. 5. Relative errors in the eigenvalue calculations for the homogeneous waveguide varied from 10^{-14} for the lowest state to 10^{-10} with approximately 2700 DOF in the global matrix, as shown in Table I.

A few comments are in order:

1. From Table I, it is clear that the eigenvalues of the homogeneous waveguide, particularly the lowest eigenvalue, show close agreement with analytical values. We note that Lee *et al.*[28] have made an analysis of the convergence of eigenvalues for hierarchical vector finite elements for waveguides. The lowest eigenvalue reported by them has an error of 10^{-12} for approximately the same number of degrees of freedom as compared with our lowest eigenvalue which has double-precision accuracy as seen in Table I.

   The lowest frequency propagating mode is the TE_{10} mode. The TE_{mn} and TM_{mn} modes with $m,n \neq 0$ are degenerate.

2. The diagonalizer delivers a linear combination of degenerate TM- and TE-modes. In order to resolve the eigenfunctions into distinct TM- and TE-modes, it is necessary to rescale one of the in-plane magnetic field components before using the in-plane components to calculate H_z and the electric field components. The need to rescale one of these components is a consequence of the fact that the in-plane field components are used to construct the global matrix, without explicitly setting H_z or E_z to zero for TM and TE modes, respectively. While for every TM mode, there exists a TE mode with the same frequency, the resulting degeneracy cannot be resolved by a simple perturbation of the waveguide cross-sectional dimensions or global matrix elements.

3. Accidental degeneracies, which involve different modes

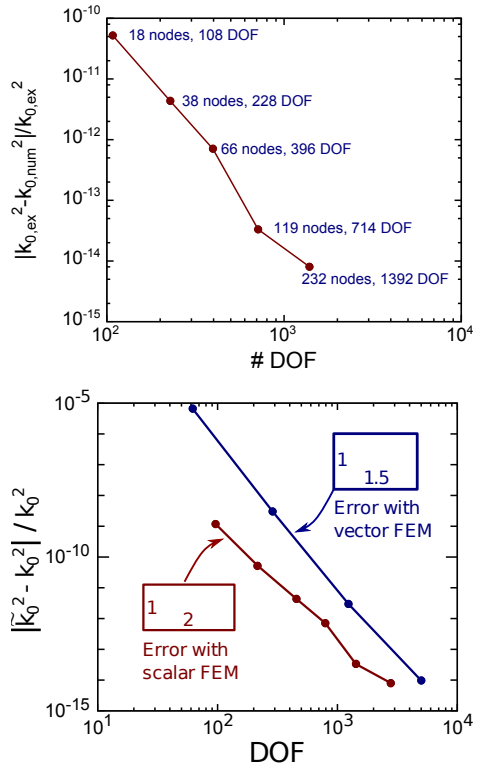

FIG. 6: The convergence of the eigenvalue for the lowest frequency, TE_{10}-mode is displayed as the global number of degrees of freedom (DOF) is increased through mesh refinement for a homogeneous waveguide. The solid curve (red) is obtained with HFEM and compared with published results using VFEM.[28] (From Boucher *et al.*, Ref. 33.)

TABLE I: Numerically calculated eigenvalues versus their predicted values for the ten lowest-energy modes of the homogeneous rectangular waveguide. The number of Hermite finite elements used was 406 with a global matrix size of 2784. (Adapted from Boucher *et al.*, Ref. 33.)

Mode	Theoretical	HFEM	Error
TE_{10}	1.024 674 011 002 72	1.024 674 011 002 69	3.0×10^{-14}
TE_{20}	1.098 696 044 010 89	1.098 696 043 949 03	6.2×10^{-11}
TE_{01}	1.098 696 044 010 89	1.098 696 044 076 11	6.5×10^{-11}
$TE_{11}+TM_{11}$	1.123 370 055 013 61	1.123 370 054 915 78	9.8×10^{-11}
$TE_{11}+TM_{11}$	1.123 370 055 013 61	1.123 370 055 117 61	1.0×10^{-10}
$TE_{21}+TM_{21}$	1.197 392 088 021 78	1.197 392 087 905 68	1.1×10^{-10}
$TE_{21}+TM_{21}$	1.197 392 088 021 78	1.197 392 088 225 77	2.0×10^{-10}
TE_{30}	1.222 066 099 024 51	1.222 066 099 118 76	9.4×10^{-11}
$TE_{31}+TM_{31}$	1.320 762 143 035 40	1.320 762 143 075 83	4.0×10^{-11}
$TE_{31}+TM_{31}$	1.320 762 143 035 40	1.320 762 143 933 56	9.0×10^{-10}

having the same frequency, may occur, especially if one dimension of the waveguide cross-section is commensurate with the other. These accidental degeneracies may be removed by introducing a small perturbation in the global matrix, and do not require any additional postprocessing.

4. We note that the transverse nature of the modes is demanded in vector finite element analysis for every element. Here we impose the transversality condition at the end of the calculation for the global eigenstates.

We now determine the convergence properties of the HFEM solutions. In Fig. 6(a), we show the convergence of the eigenfrequency to its analytically determined value in a homogeneous waveguide. For the lowest frequency TE_{10}-mode, as the global number of DOF is increased through mesh refinement, the accuracy improves steadily until 2400 DOF when the curve in red (lower curve) obtained with HFEM reaches down to 10^{-14}. The HFEM delivers an accuracy of 10^{-9} with just 96 DOFs (8 nodes). These results are extraordinary in terms of how quickly the frequency of the lowest mode is determined accurately. In the same figure, we have overlaid the VFEM data[28] in the blue curve (upper curve). At the low end of mesh refinement, with ∼100 DOF, the hierarchical VFEM employing a comparable order quintic polynomial basis has an error of $\simeq 10^{-5}$ for a hollow rectangular waveguide. With further mesh refinement leading to ∼5000 DOF the VFEM has an error comparable to our HFEM formulation with ∼2400 DOF.

We can also consider the error in the eigenvalues of the higher states. The eigenvalues of solutions above the ground state have errors approximately three to four orders of magnitude higher, but converge at the same rate as the ground state. This indicates that the derivative continuity of the fields is allowing for a high-quality variational solution even at modest discretization levels, which is the essence of FEM.

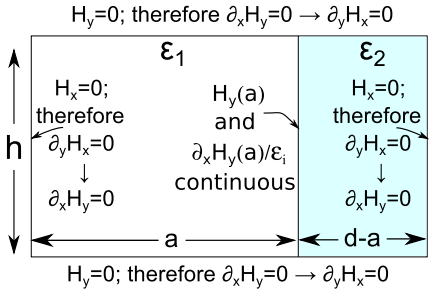

FIG. 7: The boundary conditions and dimensions for a partially filled perfectly electrically conducting (PEC) waveguide are shown. These boundary conditions were implemented in the finite element simulations.

C. HFEM results for the inhomogeneous waveguide

We now consider a partially filled waveguide with geometry and boundary conditions as shown in Fig. 7. This is an especially attractive test case for HFEM because it addresses a canonical problem for which VFEM was created, namely, the presence of spurious solutions in other scalar FEM formulations. In addition, this particular waveguide configuration shows the efficacy of using HFEM to resolve spatially varying fields of both sinusoidal and exponential (sinh and cosh) dependences. Fields of both types have analytic solutions as shown below, and therefore we can compare with analytic solutions. These field concepts are technologically important to capture with the HFEM technique because they appear in the design of slow-wave structures, on-chip waveguides, and dielectrically-loaded leaky-wave antennas. It was our expectation that HFEM would perform extremely well in resolving both types of eigenmodes because these issues are readily encountered when using scalar HFEM in the solution of quantum mechanical wavefunctions. The combination of a sine and a hyperbolic sine field solution is analogous to the quantum calculation for an asymmetric quantum well. When $(k_z^2+(n\pi/h)^2)/\varepsilon_1 < k_0^2$ this is equivalent to the potential energy of an electron in such a well being higher than the electron energy in the barrier region leading to an exponentially falling solution in the "barrier region" which

is analogous to the dielectric with permittivity ε_1. When $k_o^2 > (k_z^2 + (n\pi/h)^2)/\varepsilon_2$ sinusoidal solutions are obtained, corresponding to the confined state solutions in a quantum well. Similar analogies have been drawn previously. Not surprisingly, the symmetric potential well problem in 1D quantum mechanics has been compared with the electromagnetic confinement in a dielectric slab waveguide surrounded by air[45] as this amounts to the same problem.

We plot fields of both sinusoidal and exponential spatial variation in Fig. 8(a). The predicted longitudinal section electric (LSE, or TE to $\hat{x}$) eigenvalues are shown as functions of $\varepsilon_2/\varepsilon_1$ in Fig. 8(b). The quantum well analogy suggests that as ε_2 is increased more modes are captured by the higher dielectric region leading to the sinusoidal behavior in the larger dielectric region and an exponential decay into the lower dielectric region, as shown schematically in Fig. 8(a).

The predicted eigenvalues which correspond to longitudinal section magnetic (LSM, or TM to $\hat{x}$) modes are also shown as functions of $\varepsilon_2/\varepsilon_1$. Note that every solution undergoes a transition from the cosine-like regime to the hyperbolic regime, as shown by the color change in the plot of each eigenvalue, at a certain threshold value of the permittivity. These threshold values depend on the value of k_z and the frequency of the eigenfunctions in the y-direction. This is shown in Fig. 8.

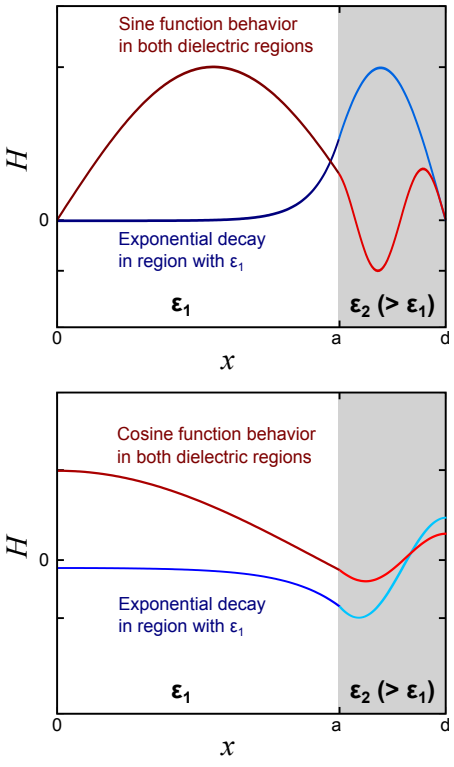

FIG. 8: Variation of the mode frequency as the dielectric ratio is increased is shown in an inhomogeneous dielectrically loaded waveguide. (a) The waveguide sustains sine/sine and sine/sinh type solutions for H_x. (b) The waveguide sustains cosine/cosine and cosine/cosh type solutions for H_y. (Adapted from Boucher *et al.*, Ref. 33.)

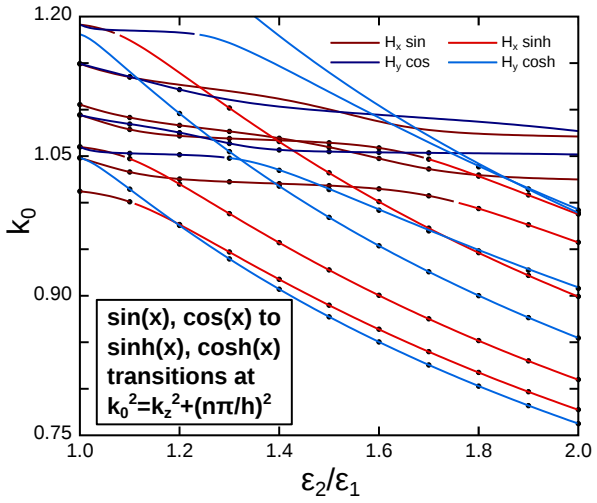

FIG. 9: Eigenvalues of several propagating modes obtained from analytic dispersion relations, are plotted along with their HFEM computed values (points) as functions of the dielectric ratio $\varepsilon_2/\varepsilon_1$, which is here limited from 1.0 to 2.0. the sine (cosine) -like solutions evolve into their hyperbolic form in the lower dielectric region as the dielectric ratio increases. (From Boucher *et al.*, Ref. 33.)

The analytically determined eigenvalues were compared to the results found using the HFEM. Eigenvalues of several propagating modes obtained from analytic dispersion relations, are plotted along with their computed values (points) as functions of the dielectric ratio $\varepsilon_2/\varepsilon_1$ in Fig. 9. The agreement between the theoretically determined eigenvalues and those calculated using HFEM is excellent. The first 10 eigenvectors in the inhomogeneous waveguide, with a dielectric constant $\varepsilon_2 = 1.5$, are shown in Figs. 9. The eigenmodes for a dielectric constant $\varepsilon_2 = 2.0$ lead to more of the modes being confined in the higher dielectric region as compared with the case where $\varepsilon_2 = 1.5$.

The HFEM correctly solves for the modes supported by partially dielectric-loaded waveguides (both slow- and fast-wave regimes; both LSE and LSM modes). Of particular importance is that the formulation can solve for these various dielectric-loaded modes without spurious solutions.

VII. CAVITY ELECTRODYNAMICS AND ACCIDENTAL DEGENERACIES

To demonstrate the capabilities of HFEM in 3D calculations, in this section we solve Maxwell's equations in a cubic cavity. Since HFEM is equally applicable to **E**-field calculations as it is to **H**-field, here we choose to work with **E**-field. Recall that the functional integral to be optimized is then of the form

$$\mathbf{L} = \int_V dV \left[\nabla \times \mathbf{E}^* \cdot \mu_r^{-1} \nabla \times \mathbf{E} - k_0^2 \mathbf{E}^* \cdot \varepsilon_r \mathbf{E} \right]. \qquad (35)$$

We note that in 3D we do not have the freedom to impose the divergence-free condition on the fields since we need to solve

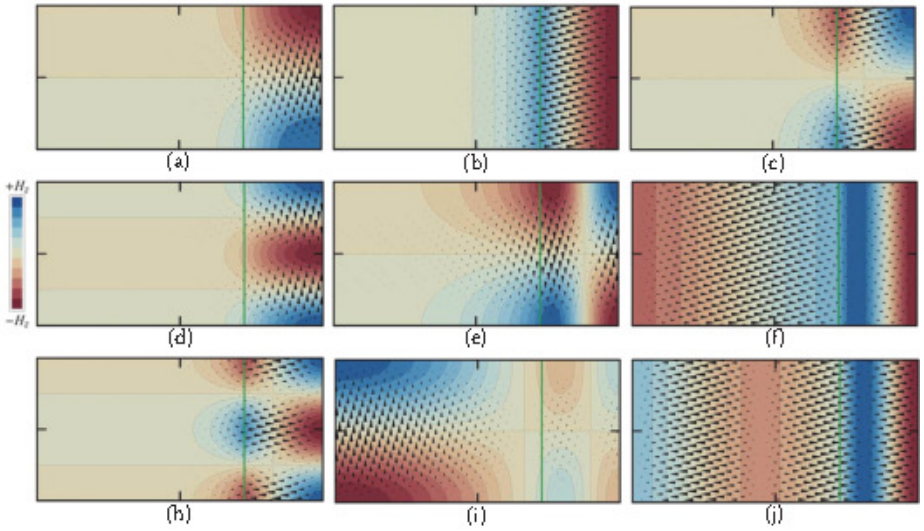

FIG. 10: Field patterns for the nine lowest frequency LSE modes an inhomogeneous 2:1 aspect ratio PEC waveguide are plotted in (a)-(j) in increasing order. The dielectric ratio was $\varepsilon_2/\varepsilon_1 = 1.5$ (region 1 is left of the vertical line, region 2 to the right) and $k_z = 1.0$. The arrows represent the in-plane H-fields, while the shading shows the H_z-field pattern. (From Boucher *et al.*, Ref. 33.)

for all three field components as opposed to only one of the components as in waveguides. So to minimize the divergence, we introduce a penalty term $\lambda \left|\nabla \cdot \varepsilon_r \mathbf{E}\right|^2$ in the functional $\mathbf{L}$, given by

$$\mathbf{L} = \int_V dV \Big[\nabla \times \mathbf{E}^* \cdot \mu_r^{-1} \nabla \times \mathbf{E} - k_0^2 \mathbf{E}^* \cdot \varepsilon_r \mathbf{E} + \lambda \left|\nabla \cdot \varepsilon_r \mathbf{E}\right|^2 \Big], \tag{36}$$

where λ is the Lagrange multiplier. The fields are represented by Hermite interpolation polynomials on hexahedral elements multiplied by the values of fields and their derivatives at the vertices (nodes) of each element. The integral can be discretized over the elements to obtain a matrix equation in terms of the nodal parameters. We invoke the principle of stationary action, and set the variation of $\mathbf{L}$ with respect to $\mathbf{E}^*$ equal to zero. This yields a generalized eigenvalue problem which is solved to obtain the frequencies and field distributions of the resonating modes. The magnetic fields are readily obtained from the electric fields using Maxwell's equations.

We consider a cubic cavity with perfectly conducting metallic boundaries. We assume that the dielectric regions of the cavity are charge-free and current-free. At the surface of a perfect electrical conductor, the electric and magnetic fields satisfy the boundary conditions (BCs)[46–48]

$$\hat{\mathbf{n}} \times \mathbf{E} = 0 \qquad \text{and} \qquad \hat{\mathbf{n}} \cdot \mathbf{H} = 0. \tag{37}$$

These relations give the BCs on the periphery of the cavity. When working with electric fields, the tangential components of the field are set to zero at the boundary, while the normal components are determined variationally.

A. Origin and nature of spurious solutions

Numerical solutions of Maxwell's equations are polluted with non-physical spurious solutions. The divergence of Eq. 1 leads to

$$k_0^2 \nabla \cdot \varepsilon_r \mathbf{E} = 0. \tag{38}$$

This condition is satisfied when either $k_0 = 0$ or $\nabla \cdot \varepsilon_r \mathbf{E} = 0$. In theory, these spurious solutions have zero frequency. However, due to discretization, the eigenvalues of the spurious modes are not computed exactly as zero, and can have numerical values comparable to those of the physical solutions. Consequently, the spurious eigenvalues cannot be easily separated from the desired eigenvalues.[6,9] When the divergence condition is not satisfied, it implies the present of charges inside the cavity. Examples of spurious solutions obtained when the divergence condition is not imposed are shown in Fig. 11. Note how the field distribution shows source-like behavior within the cavity, indicative of non-zero divergence. For the time-harmonic problem, spurious solutions have zero curl and a finite divergence. This manifests numerically as a very large divergence-to-curl ratio, compared to physically admissible solutions. In the following section we show within our HFEM approach we can increase this ratio with increase in the mesh density. We use this criterion to filter out spurious solutions from the physical admissible solutions.

B. The penalty method and the zero-divergence constraint

The penaly method[39] has been proposed to remove spurious solutions in nodal finite element implementations. The penalty term pushes most spurious eigenfrequencies outside

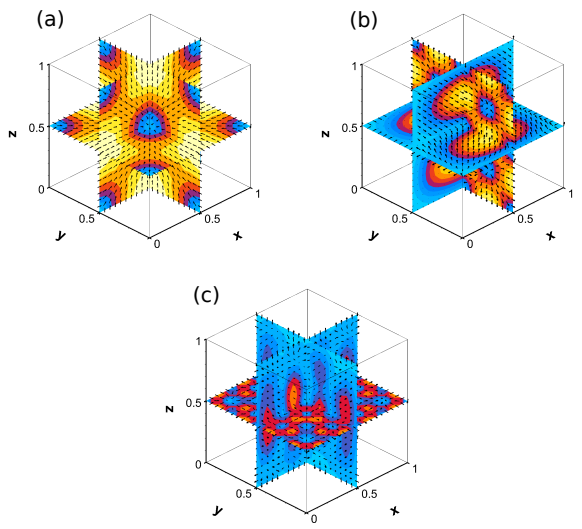

FIG. 11: Spurious solutions in the empty cubic cavity of unit dimensions. Note the field distribution, which is indicative of the presence of sources, even though the cavity is empty. Light yellow(gray) regions correspond to amplitude antinodes, and blue(darker) regions correspond to amplitude nodes. (Adapted from Pandey *et al.*, Ref. 38.)

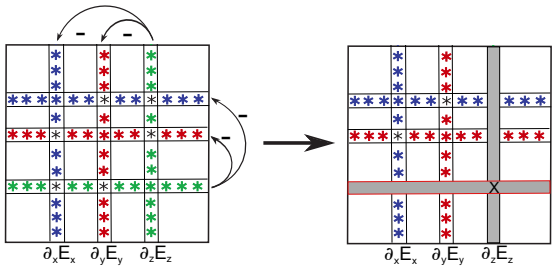

FIG. 12: Explicity imposing the divergence-free condition by performing global matrix row and column operations. One of the derivative DOF is eliminated in favor of the remaining two. Here $X = 1$ for the left-hand side matrix, and X is set to a large value in the right-hand side matrix, in the generalized eigenvalue problem. This choice of a large number pushes the eigenvalue of the redundant 1×1 subspace out of the spectral range of interest.

the spectral range of interest. However, a fixed Lagrange multiplier does not remove all spurious modes. A low value of the penalty factor leaves behind some spurious modes, and a large value of the penalty factor causes errors in the eigenvalues. One proposed algorithm is to use a different multiplier for each mode.[21] This, however, is an expensive iterative scheme. On the other hand, a constant penalty offers an inexpensive method for removing most of the zero-frequency spurious modes, and can be further enhanced. In our calculation, we use a fixed Lagrange multiplier, $\lambda = 1$.

One key feature of spurious modes is a large divergence-to-curl ratio $|\nabla \cdot \mathbf{E}|/|\nabla \times \mathbf{E}|$.[21] There is then the possibility of identifying and removing any remaining spurious solutions based on this ratio, after we determine the eigenfields. However, the divergence-to-curl ratio for spurious and physically admissible modes can become comparable, as seen in the first and second columns of Table II. It is clear that the penalty factor alone does not eliminate all the spurious solutions. There still are spurious solutions that can intermix with the physically acceptable solutions. Note that the Hermite shape functions supports a non-zero divergence value within the brick volume.

We resolve this issue by explicitly imposing the divergence-free condition at each node, using the derivative degrees of freedom.[41,42,49] At the matrix level, one of the terms in the zero-divergence condition, $\nabla \cdot \varepsilon_r \mathbf{E} = 0$, is eliminated in favor of the other two. The procedure is demonstrated in Fig. 12 for the simpler case of a constant ε_r. Applying this technique drives the divergence-to-curl ratio of physically admissible solutions even lower, and that of spurious solutions higher, as can be seen from the third and fourth columns of Table II. A comparison of columns 2 and 4 in this table show the enhancement of the ratio $|\nabla \cdot \mathbf{E}|/|\nabla \times \mathbf{E}|$ for spurious solutions, and a substantial reduction of this ratio for the physical solutions.

Additionally, since the divergence condition is applied at each node, the total divergence of the physically admissible solutions decreases further with mesh refinement, whereas it increases considerably for spurious solutions (see columns 4 and 6 in Table II). This is manifested as the element size is reduced, and the interpolation from the nodes having the divergence-free condition into the interior of the elements is more effective with increasing mesh density.

This is in contrast to VFEM, where the normal discontinuity of edge elements leads to the formation of artificial charges at element interfaces, thus increasing the total divergence of the solutions; this problem worsens with mesh refinement.[50] Note that in VFEM, the zero-frequency spurious solutions are separated by filtering out the null-space of the curl operator from the spectrum using iterative techniques,[51,52] or by finding eigenvalues in the interior of the spectrum. This is necessary, since if the physical solution space is not normal to the null space, the physical solutions will be polluted by null vectors.

We also report the results for HFEM when tetrahedral elements are used. The eigenvalues, along with the corresponding divergence-to-curl ratios are listed in Table III. The number of degrees of freedom in this calculation is 42438. As can be seen in the divergence-to-curl values in Table III, using tetrahedral elements for the breaking of the cavity, imposing the penalty factor alone does not fully separate the physical solutions from spurious solutions. Note also from Table III that both the penalty factor and the divergence-free condition drastically improves the tagging of spurious solutions. We observe less number of spurious solutions polluting the spectrum as compared to the cubic elements. Another feature observed is that the eigenvalues of the spurious solutions are distinct from those of the physical solutions, as compared to the cubic element case, where the spurious solutions are degenerate with the physical ones.

TABLE II: The enhancement of the global divergence-to-curl ratio, for the lowest few eigenstates, by imposing the divergence-free condition at each node at the element matrix level are listed. The Hermite elements are defined over a 27-node cubic element with a total of 216 DOFs. (From Pandey *et al.*, Ref. 38.)

Penalty factor method only		Penalty factor with $\nabla\cdot\mathbf{E} = 0$ condition				Solution Type
DOF: 8232		DOF: 8232		DOF: 52728		
k_0^2	$\lvert\nabla\cdot\mathbf{E}\rvert/\lvert\nabla\times\mathbf{E}\rvert$	k_0^2	$\lvert\nabla\cdot\mathbf{E}\rvert/\lvert\nabla\times\mathbf{E}\rvert$	k_0^2	$\lvert\nabla\cdot\mathbf{E}\rvert/\lvert\nabla\times\mathbf{E}\rvert$	
19.739334159	0.000000000	19.739221048	0.000000000	19.739209007	0.000000000	Physical
19.739334159	0.000000000	19.739221048	0.000000000	19.739209007	0.000000000	Physical
19.739334159	0.000000000	19.739221048	0.000000000	19.739209007	0.000000000	Physical
29.609001232	0.005891138	29.608831573	0.000000197	29.608813510	0.000000003	Physical
29.609001232	0.000389894	29.608831573	0.000000197	29.608813510	0.000000003	Physical
29.609001232	172.872234679	31.328579414	220.518451137	31.501166266	545.498991584	Spurious
49.358373749	0.000000000	49.349260110	0.000000000	49.348046601	0.000000000	Physical
49.358373749	0.000000000	49.349260110	0.000000000	49.348046601	0.000000000	Physical
49.358373749	0.000000000	49.349260110	0.000000000	49.348046601	0.000000000	Physical
49.358373749	0.000000000	49.349260110	0.000000000	49.348046601	0.000000000	Physical
49.358373749	0.000000000	49.349260110	0.000000000	49.348046601	0.000000000	Physical
49.358373749	0.000000000	49.349260110	0.000000000	49.348046601	0.000000000	Physical
59.228040826	0.572767636	59.218870635	0.000006213	59.217651104	0.000000056	Physical
59.228040826	0.575823907	59.218870635	0.000006195	59.217651104	0.000000080	Physical
59.228040826	0.137630780	59.218870635	0.000006005	59.217651104	0.000000112	Physical
59.228040826	0.135054548	59.218870635	0.000006204	59.217651104	0.000000094	Physical
59.228040826	0.000065277	59.218870635	0.000004082	59.217651104	0.000000043	Physical
59.228040826	0.277005817	59.218870635	0.000008226	59.217651104	0.000000129	Physical
59.228040826	1.063357739	62.432033897	167.942572387	62.873334761	321.742164741	Spurious
59.228040826	1.083589808	62.432033897	167.942572387	62.873334761	321.742164741	Spurious
59.228040826	3.580885859	62.432033897	167.942572387	62.873334761	321.742164741	Spurious

C. Fields in an empty cubic cavity

To demonstrate our method, we first model an empty cubic cavity with conducting boundaries, with $\varepsilon_r = 1$ and $\mu_r = 1$ inside. Consider a cavity of unit dimensions. These calculations are done using HFEM, with 8232 DOFs, within a parallel computing environment.[53–55]

From Table IV, it is clear that the eigenvalues of the empty cavity obtained through our scheme have very small errors, when compared to the analytical values. In Fig. 13, we show the convergence of the calculated frequencies to their analytical values in an empty cube of unit dimensions for both HFEM and VFEM (obtained using the software package MFEM[37]). As the global number of DOFs is increased through mesh refinement, the accuracy improves steadily. Quintic HFEM delivers an accuracy of 1 part in 10^9 with just 8232 DOFs. The second curve from bottom (in green) obtained using 5th order VFEM shows about 10 times larger error for comparable DOFs. Even with further mesh refinement, VFEM has an error higher than our HFEM scheme. HFEM gives a higher accuracy than VFEM, even with half the number of DOFs. This reduction in required number of DOFs leads to improvement in computation time.

The matrix bandwidth is defined as the sum of sub- and supradiagonal arrays together with the main diagonal. For a total of 8232 DOFs (52728 DOFs), the cubic Hermite polynomials utilize a bandwidth of 16175 (105167), while the quintic Hermite interpolation polynomials occupy a comparable bandwidth of 16223 (105167). The occupancy of a matrix is defined as the percentage of nonzero entries in the matrix. While going from the cubic to quintic Hermite polynomials, there is only a nominal increase in the matrix occupancy from 0.04% to 0.125% for a matrix of dimensions 8232 × 8232. With an increase in DOFs to 52728, the occupancy decreases further to 0.0083% for the cubic Hermite, and is 0.025% for the quintic Hermite interpolation polynomials. In the case of cubic Hermite interpolation polynomials, with 60 processors, matrices of dimensions 8232 × 8232 (52728 × 52728) are assembled in 4.9 minutes (50.9 minutes), and diagonalized in 6.2 minutes (41.2 minutes), whereas using the quintic Hermite interpolation polynomials, with the same number of processors, matrices of the same dimensions are assembled in 66.4 minutes (471.4 minutes), and diagonalized in 9.6 minutes

TABLE III: The enhancement of the global divergence-to-curl ratio, for the lowest few eigenstates, by imposing the divergence-free condition at each node at the element matrix level are listed. The Hermite polynomials here are defined over a tetrahedral element with the 4 vertex nodes with 10 DOFs, and 4 face-centered nodes with 4 DOFs, resulting in a total of 56 DOFs for each element. The eigenmodes are obtained using 42438 DOFs.

Penalty factor method only		Penalty factor with $\nabla\cdot\mathbf{E}=0$ condition		Solution
k_0^2	$\lvert\nabla\cdot\mathbf{E}\rvert/\lvert\nabla\times\mathbf{E}\rvert$	k_0^2	$\lvert\nabla\cdot\mathbf{E}\rvert/\lvert\nabla\times\mathbf{E}\rvert$	type
19.739208827	0.000000000	19.739208827	0.000000000	Physical
19.739208829	0.000000000	19.739208829	0.000000000	Physical
19.739208848	0.000000000	19.739208849	0.000000000	Physical
29.608813476	0.486030689	29.608813484	0.000000002	Physical
29.608813484	0.486018524	29.608813497	0.000000002	Physical
29.608813497	0.495455431	41.117998502	8.090436581	Spurious
49.348030093	0.000000045	49.348030229	0.000000041	Physical
49.348030963	0.000000051	49.348031125	0.000000045	Physical
49.348032032	0.000000054	49.348032161	0.000000046	Physical
49.348032074	0.000000058	49.348032241	0.000000049	Physical
49.348032134	0.000000059	49.348032302	0.000000051	Physical
59.217642131	0.274980399	59.217643847	0.000000072	Physical
59.217644056	0.242246173	59.217645045	0.000000080	Physical
59.217645004	0.230927738	59.217654541	0.000000124	Physical
59.217652841	0.276708712	59.217656977	0.000000135	Physical
59.217654456	0.287009378	59.217657319	0.000000137	Physical
59.217655419	0.276443701	59.217657643	0.000000135	Physical
59.217656808	0.635597226	N/A	N/A	Spurious
59.217657209	0.834678138	N/A	N/A	Spurious
59.217657452	0.856486293	N/A	N/A	Spurious

(78.6 minutes). The time taken can be reduced by optimizing the number of processors used for the calculation. We have used the Krylov-Schur algorithm as implemented in SLEPc[53] for the calculations. We also consider the error in eigenvalues of higher frequency modes in Fig. 13. The errors converge at the same rate as the error in the first mode.

We note that while modeling cavities with curved boundaries, we can discretize the curved regions with tetrahedral elements. As shown in Table III, we will still be able to maintain a similar level of accuracy in field calculations.

D. Accidental degeneracies in EM cavities

Physical properties arising from the symmetry of the system can be treated efficiently using group representation theory. It has been well appreciated in quantum mechanics that the degeneracies in the energy spectrum arise from the symmetry group of the corresponding Hamiltonian.[56,57] The degeneracy of an eigenvalue is equal to the dimensionality of the corresponding irreducible representation of the symmetry group. If we have any other additional degeneracy in the spectrum which cannot be explained by the obvious geometrical symmetry of the system, it is labeled as "accidental degeneracy." In this section we discuss the presence of such accidental degeneracy and its removal for EM modes in a cavity. Pedagogical remarks on accidental degeneracy are given in Sec. VII F.

Let G be a group of order g and $\Gamma^{(i)}$ be an l_i-dimensional representation of G. For a group element R in G, its representation is given by a $l_i \times l_i$ square matrix $\Gamma^{(i)}(R)$. Then the projection operator[56] corresponding to $\Gamma^{(i)}$ is given by

$$\mathscr{P}^{(i)} = \frac{l_i}{g}\sum_R \chi^{(i)}(R)\cdot P_R, \tag{39}$$

where $\chi^{(i)}(R)$ is the character and P_R is the operator corresponding to the element R. The transformation of electric fields under the operation P_R is defined by

$$P_R\cdot\mathbf{E}(r) = R\cdot\mathbf{E}\left(R^{-1}\cdot r\right). \tag{40}$$

The projection operator $\mathscr{P}^{(i)}$ projects out the part of the field $\mathbf{E}$ that belongs to the representation $\Gamma^{(i)}$.

The electric or magnetic fields corresponding to a degenerate eigenfrequency will form *a set of vector basis-functions for the irreducible representations of the symmetry group.* Previously, we have derived a coefficient formula to recognize the irreducible representation corresponding to an eigenenergy, and obtain the symmetry adapted wavefunctions in quantum dots.[34] An analogous coefficient formula exists even in the context of electric (magnetic) modes in EM cavities. Let $\{\mathbf{E}_i\}_{i=1}^n$ be the set of eigenfields for the physical system under

TABLE IV: Eigenvalues for the forty lowest frequency modes of the empty cubic cavity, calculated numerically using Hermite interpolation polynomials are listed. The eigenvalues are compared with their analytical values and the absolute errors are displayed. (From Ref. 38.)

Mode	Degeneracy	Analytical	Hermite FEM	Error
$(0,1,1)$	3	19.7392088021787	19.7392088021791	4.4×10^{-13}
$(1,1,1)$	2	29.6088132032680	29.6088132032692	1.2×10^{-12}
$(0,1,2)$	6	49.3480220054467	49.3480220078586	2.4×10^{-9}
$(1,1,2)$	6	59.2176264065361	59.2176264089494	2.4×10^{-9}
$(0,2,2)$	3	78.9568352087148	78.9568352135412	4.8×10^{-9}
$(1,2,2)$	6	88.8264396098042	88.8264396146369	4.8×10^{-9}
$(0,1,3)$	6	98.6960440108935	98.6960442784766	2.6×10^{-7}
$(1,1,3)$	6	108.5656484119829	108.5656486795616	2.6×10^{-7}
$(2,2,2)$	2	118.4352528130723	118.4352528203570	7.2×10^{-9}

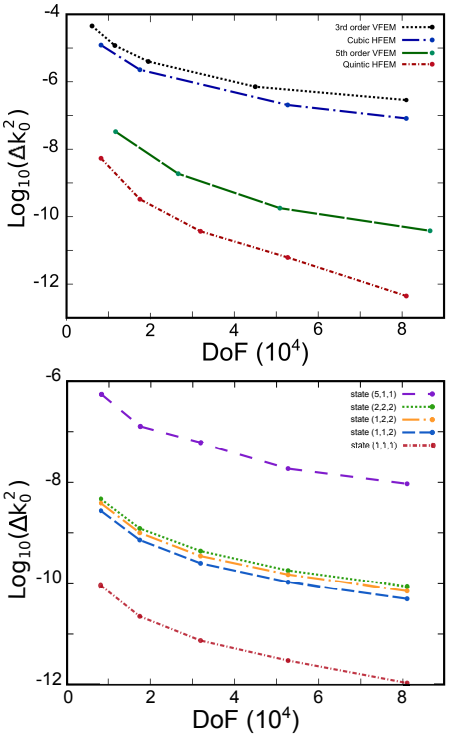

FIG. 13: The convergence of errors in eigenvalues of (a) the first mode for the 3rd order VFEM, 5th order VFEM, Hermite, and Hermite interpolation polynomials, and (b) the higher frequency modes for HFEM only are shown for the case of an empty cubic cavity of unit dimensions. Using Hermite interpolation polynomials we can reduce the error in the first mode upto 10^{-9} with just 27 elements and 8232 DOFs, with further reduction in error possible with mesh refinement. The total DOFs corresponds to the global matrix dimension.

consideration. Then the coefficient formula[34] is given by

$$c_{jk}^{(i)} = \int_V d^3r\, \mathbf{E}_j^\dagger \cdot \left(\mathscr{P}^{(i)}\mathbf{E}_k\right). \tag{41}$$

If the coefficient is nonzero, then the field $\mathbf{E}_k$ has a component in the i^{th}-representation and $\mathbf{E}_j$ is a partner. Using these coefficients we can construct the symmetry-adapted electric (magnetic) fields which are exclusively in the i^{th}-representation.

In case of an empty cubic cavity resonator of length a with conducting boundaries. The eigenmodes supported by the cubic resonator have the eigenvalues

$$k_0^2 = \left(n_1^2+n_2^2+n_3^2\right)\frac{\pi^2}{a^2}, \tag{42}$$

and the electric field components are given by

$$\begin{aligned} E_x &= E_{0x}\cos\left(\frac{n_1\pi x}{a}\right)\sin\left(\frac{n_2\pi y}{a}\right)\sin\left(\frac{n_3\pi z}{a}\right);\\ E_y &= E_{0y}\sin\left(\frac{n_1\pi x}{a}\right)\cos\left(\frac{n_2\pi y}{a}\right)\sin\left(\frac{n_3\pi z}{a}\right);\\ E_z &= E_{0z}\sin\left(\frac{n_1\pi x}{a}\right)\sin\left(\frac{n_2\pi y}{a}\right)\cos\left(\frac{n_3\pi z}{a}\right), \end{aligned} \tag{43}$$

where n_1, n_2, n_3 are non-zero integers, and E_{0x}, E_{0y}, E_{0z} are the field amplitudes in each direction.

Three kinds of degeneracies can be identified in the spectrum. The first kind is due to the permutation of mode numbers. The second kind is a consequence of the divergence-free condition $\nabla\cdot\mathbf{E}=0$. On substituting Eq. (43) in the divergence-free condition we obtain the constraint $n_1E_{0x}+n_2E_{0y}+n_3E_{0z}=0$. Hence, if $n_1,n_2,n_3\neq0$ we see that there are two independent field components; hence for a given mode (n_1,n_2,n_3) we will have at least 2 degenerate field solutions.[44] The third kind occurs when two disitinct sets of mode numbers give the same frequency, occurring when the following relation is satisfied:

$$n_1^2+n_2^2+n_3^2 = m_1^2+m_2^2+m_3^2, \tag{44}$$

TABLE V: Different possible even and odd combinations of eigenmodes in an empty cubic cavity, their degeneracy, and corresponding irreducible representations for the symmetry group O_h are listed. Here the indices m,n and ℓ are non-zero integers. (Adapted from Ref. 38.)

Mode number	Degeneracy	Irreducible representations
$(0,2n-1,2n-1)$	3	T_{1u}
$(0,2n-1,2m)$	6	$T_{1g}\oplus T_{2g}$
$(0,2n,2n)$	3	$A_{2u}\oplus E_u$
$(0,2n-1,2m-1)$	6	$T_{1u}\oplus T_{2u}$
$(0,2n,2m)$	6	$A_{1u}\oplus A_{2u}\oplus 2E_u$
$(2n-1,2n-1,2n-1)$	2	E_g
$(2n,2n,2n)$	2	E_u
$(2n-1,2n-1,2m)$	6	$T_{1u}\oplus T_{2u}$
$(2n,2n,2m-1)$	6	$T_{1g}\oplus T_{2g}$
$(2m-1,2n-1,2n-1)$	6	$A_{1g}\oplus A_{2g}\oplus 2E_g$
$(2m,2n,2n)$	6	$A_{1u}\oplus A_{2u}\oplus 2E_u$
$(2n-1,2m-1,2\ell)$	12	$2T_{1u}\oplus 2T_{2u}$
$(2n,2m,2\ell-1)$	12	$2T_{1g}\oplus 2T_{2g}$
$(2m,2n,2\ell)$	12	$2A_{1u}\oplus 2A_{2u}\oplus 4E_u$
$(2m-1,2n-1,2\ell-1)$	12	$2A_{1g}\oplus 2A_{2g}\oplus 4E_g$

with $n_i \neq m_i$, for $i = 1,2,3$.

We know that the cubic cavity has the geometrical symmetry of O_h. In Table V, we list all different possible combinations of mode numbers and their corresponding irreducible representations from the symmetry group O_h. Here, we have accounted for only the first two kinds of degeneracies. For most of the combinations of mode numbers we observe accidental degeneracy since they belong to two or more distinct irreducible representations. The accidental degeneracy associated with permutation of mode numbers can be rendered normal by identifying the existence of two dynamical operators $\Omega = (\Omega_1, \Omega_2)$, given by[38]

$$\begin{aligned} \Omega_1 &= \left(\partial_x^2 - \partial_y^2\right) \\ \Omega_2 &= \left(2\,\partial_z^2 - \partial_x^2 - \partial_y^2\right) \end{aligned} \tag{45}$$

which connect the degenerate field solutions.[58] The full covering group in this case is $\mathscr{G} = O_h \otimes \Omega$.

As described in the following section, the larger symmetry group $\mathscr{G}$ of the cavity is reduced to O_h by introducing a concentric cubic dielectric inclusion inside the cavity. This inclusion removes the accidental degeneracy due to the way the fields occupy the corner regions exterior to the cubic dielectric.

E. Fields in dielectrically loaded cubic cavity

We consider a cubic conducting cavity of dimensions $1 \times 1 \times 1$ mm^3. This cavity is loaded with a concentric cubic dielectric inclusion, of dimensions $0.5 \times 0.5 \times 0.5$ mm^3, and permittivity ε_2, as shown in Fig. 14. The permittivity in the rest of cavity is ε_1. The eigenvalues of the first few modes are tabulated for the dielectric ratios $\varepsilon_2/\varepsilon_1 = 1.2$ and $\varepsilon_2/\varepsilon_1 = 5.0$. The calculations are done with 17576 DOFs, to accurately model the dielectric function.

In Figs. 15–16 we show electric field distributions for the first few modes in the loaded cavity with $\varepsilon_2/\varepsilon_1 = 1.2$. As shown in Fig. 15, the first three modes in the loaded cavity remain degenerate, and they belong to the three dimensional representation T_{1u} of the group O_h. An instance of the removal of accidental degeneracy can be seen in the $(1,1,3),(1,3,1),(3,1,1)$ modes, which in the empty cubic cavity are part of a degenerate sextuplet which belong to the

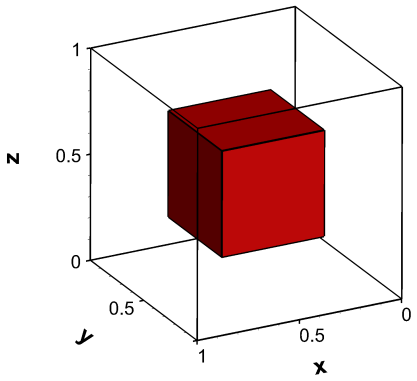

FIG. 14: Schematics of a dielectrically loaded cavity with O_h symmetry. The external conducting cavity has dimensions $1\times1\times1$ mm^3; the cubic dielectric loading has dimensions $0.5\times0.5\times0.5$ mm^3, with dielectric constant ε_2. The permittivity in the rest of cavity is ε_1.

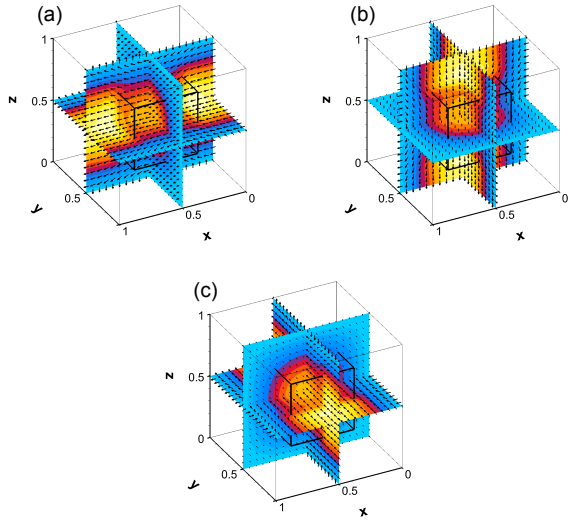

FIG. 15: The symmetry-adapted triplet states $(0,1,1)$, $(1,0,1)$, $(1,1,0)$ of the dielectrically loaded cavity with an eigenvalue $k_0^2 = 18.5267$ are shown in (a), (b) and (c), respectively. The inserted cubic dielectric has dimensions $0.5\times0.5\times0.5$ mm^3, with a dielectric constant $\varepsilon_2/\varepsilon_1 = 1.2$. Light yellow (gray) regions correspond to amplitude antinodes, and blue (darker) regions correspond to amplitude nodes. (From Pandey *et al.*, Ref. 38.)

$A_{1g}\oplus A_{2g}\oplus 2E_g$ representation (see Table V). This sextuplet decomposes into four separate irreducible representations. In Figs. 16(a,b), we show the singlet modes in the loaded cavity belonging to the irreducible representations A_{1g} and A_{2g}, respectively. We note that in Fig. 16(b) the magnitude of the electric field has complete O_h symmetry, while the vectors flip their directions under an inversion. Similarly, Figs. 16(c,d) and 16(e,f) show symmetry-adapted partners, which belong to the two dimensional representations E_g.

In Fig. 20, the evolution of mode frequency on varying the dielectric constant ε_2 in the interior is shown for the lowest few modes. We observe level crossings akin to the case of bound states in a finite quantum well as the well depth is varied.[34] In Figs. 17, we plot the surface currents on the conducting cavity. These currents ensure that the magnetic field outside the cube is identically zero. Note that the surface currents are symmetry-adapted as well.

As a final example, we consider a linear z-dependent perturbation to the dielectric function in the interior dielectric block. This perturbation reduces the symmetry group of the loaded cavity from O_h to C_{4v}, resulting in a further reduction in mode degeneracies. In Table VII, we have listed the eigenfrequencies obtained with our method, and classified them into corresponding irreducible representations of the group C_{4v}. In Fig. 18 we show electric field distributions for the degenerate modes $(1,1,1)$ in the loaded cubic cavity. In Fig. 19, we show electric field distributions for the same modes, but for a perturbed cavity. Note how the modes in the perturbed case are now non-degenerate and split in frequency. As seen from Fig. 19, the electric field magnitudes have complete C_{4v} symmetry; the first mode belongs to the representation A_1 of C_{4v}, while the second mode belongs to the representation B_1.

Quality factor: A classic benchmark in computational electromagnetics is to obtain the Q-factor in a resonant cavity with lossy walls. Here we calculate the Q-factor in a loaded cavity which has contributions from a) the dissipation of energy at the cavity walls, and b) the dielectric loss when the permittivity has both real and imaginary parts, $\varepsilon = \varepsilon_r + i\varepsilon_i$. For the dielectric losses, the Q-factor associated with the resonator[46,59] is given by

$$Q_d = \frac{\iiint_V dV\ \varepsilon_r |\mathbf{E}|^2}{\iiint_V dV\ \varepsilon_i |\mathbf{E}|^2}. \tag{46}$$

We note that when a constant dielectric loading fills the entire cavity we obtain $Q_d = \varepsilon_r/\varepsilon_i$, irrespective of the eigenfrequency. We have verified this in the limit of full dielectric occupancy. In Table VIII, we have shown the eigenvalues and their corresponding Q_d values in a partially loaded cubic cavity with $\varepsilon_r = 2$ and $\varepsilon_i = 10^{-6}$. The degeneracy spectrum again follows O_h symmetry.

When the cavity resonator has imperfect conducting walls, we define the corresponding quality factor[47] as

$$Q_c = \omega\sigma\delta_s \frac{\iiint_V dV\ \mu |\mathbf{H}|^2}{\oiint_{\substack{\text{cavity}\\ \text{walls}}} dS\ |\mathbf{n}\times\mathbf{H}|^2}, \tag{47}$$

where σ is the conductivity of the metallic surface and δ_s is the skin depth at the resonant frequency ω. In Table VIII, we list the Q_c values at the resonant frequencies in a partially loaded cubic cavity with gold boundary walls.

TABLE VI: Numerically calculated eigenvalues for the lowest few frequency modes of the dielectrically loaded cubic cavity with 17576 total DOFs using quintic Hermite interpolation polynomials. The column labeled "irrep" corresponds to the irreducible representation the multiplet belongs to. The conducting cavity has dimensions $1 \times 1 \times 1$ mm^3; the cubic dielectric loading has dimensions $0.5 \times 0.5 \times 0.5$ mm^3. The eigenvalues are compared against their values for the modes in the empty cavity of unit dimensions. (From Pandey *et al.*, Ref. 38.)

Mode number	"Irrep"	k_0^2		
		$\varepsilon_2/\varepsilon_1 = 5.0$	$\varepsilon_2/\varepsilon_1 = 1.2$	$\varepsilon_2/\varepsilon_1 = 1.0$
$(0,1,1),(1,0,1),(0,1,1)$	T_{1u}	7.919791186	18.526768246	19.739208802
		7.919791186	18.526768246	19.739208802
		7.919791186	18.526768246	19.739208802
$(1,1,1)$	E_g	18.202154429	28.899507681	29.608813203
		18.202154429	28.899507681	29.608813203
$(0,1,2),(2,1,0)$	T_{1g}	21.354532231	47.387744521	49.348022007
		21.354532231	47.387744521	49.348022007
$(1,0,2),(2,0,1)$		21.354532231	47.387744521	49.348022007
	T_{2g}	23.416822776	47.404561358	49.348022007
$(0,2,1),(1,2,0)$		23.416822776	47.404561358	49.348022007
		23.416822776	47.404561358	49.348022007
$(1,1,2),(2,1,1)$	T_{1u}	35.614536102	57.284302371	59.217626408
		35.614536102	57.284302371	59.217626408
$(2,1,1),(1,1,2)$		35.614536102	57.284302371	59.217626408
	T_{2u}	38.219214013	58.327254711	59.217626408
$(1,2,1),(1,2,1)$		38.219214013	58.327254711	59.217626408
		38.219214013	58.327254711	59.217626408
$(0,2,2),(2,0,2),(2,2,0)$	E_u	38.305292320	76.979818578	78.956835213
		38.305292320	76.979818578	78.956835213
	A_{2u}	42.790037374	77.001769904	78.956835213
$(1,1,3),(1,3,1),(3,1,1)$	$2E_g$	55.137384588	103.727559345	108.565648679
		55.137384588	103.727559345	108.565648679
		77.568304705	107.596740348	108.565648679
		77.568304705	107.596740348	108.565648679
	A_{1g}	67.549698454	107.431515611	108.565648679
	A_{2g}	77.460283215	107.591198480	108.565648679

F. Remarks on the accidental degeneracy

Let $\tilde{G}$ be an infinitesimal transformation for the coordinate system. Given a Hamiltonian $\hat{H}$, if $[\tilde{G},\hat{H}] = 0$, and $\tilde{G}$ does not explicitly depend on time, then we say that $\tilde{G}$ is a constant of motion. Such constants of motion generate symmetries since they transform one eigenstate to another of the same eigenvalue. We expect to find additional constants of motion whenever we observe accidental degeneracies as explained below. If the Hamiltonian is separable in a coordinate system, then the separation constants may be considered as constants of motion.[60] These are just the generators of the additional symmetry operations. Typically, accidental degeneracies are then rendered normal by identifying the hidden covering group.

The example of the familiar hydrogen atom best illustrates the symmetry argument. In the H-atom, with its Coulomb potential having geometrical rotational symmetry, the conservation of the 3 components of angular momentum provide us three constants of motion associated with the 3D rotation group $O(3)$. Equivalently, we consider the angular momentum components $\{L_+, L_-, L_z\}$ as the set of 3 operators which commute with the Hamiltonian of the H-atom. We know that an eigenstate $|E,\ell,m\rangle$ of the H-atom transforms under the operation of ladder operators as

$$L_\pm |E,\ell,m\rangle = \sqrt{(\ell \mp m)(\ell \pm m + 1)}\, |E,\ell,m \pm 1\rangle\,. \qquad (48)$$

Hence angular momentum operators transform degenerate eigenstates of the same ℓ but of different azimuthal quantum numbers m into one another. For a given ℓ we find that $(2\ell+1)$ states are degenerate. However the eigenstates of different allowed ℓ are also degenerate here, leading to a textbook example of accidental degeneracy. Fock[61] identified the

TABLE VII: Lowering of symmetry, and splitting of mode degeneracy in the presence of a dielectric inclusion that has a preferential z-axis. (From Pandey *et al.*, Ref. 38.)

O_h	C_{4v}	k_0^2
T_{1u}	A_1	14.840987
	E	14.841426
		14.841426
E_g	A_1	26.303562
	B_1	26.309544
T_{1g}	A_2	39.928882
	E	39.937310
		39.937310
T_{2g}	B_2	40.430146
	E	40.431522
		40.431522
T_{1u}	A_1	51.226115
	E	51.202143
		51.202143
T_{2u}	B_1	54.625215
	E	54.631936
		54.631936
E_u	A_2	68.152735
	B_2	68.160536
A_{2u}	B_2	68.993259

hidden four-dimensional rotational symmetry group $O(4)$ as the true symmetry of the H-atom, which explains these additional degeneracies manifesting as the familiar $s, p, d, f, \ldots$ states being degenerate for a given principal quantum number n. We expect to find additional operators (constants of motion) which commute with the Hamiltonian and connect eigenstates of different ℓ quantum numbers. These operators are just the three components of the conserved Runge-Lenz vector, ,[62] A, which transform degenerate eigenstates of different ℓ quantum numbers into one another,[63] analogous to Eq. (48). The components of the angular momentum L and the Runge-Lenz vector A generate the symmetry group $O(4)$. We note that even though the components of L and A commute with the Hamiltonian, they will not mutually commute with each other. These components are subject to kinematic constraints of the Casimir operators for the group $O(4)$.[64] Hence the eigenstates of the Hamiltonian are represented by the complete set of commuting operators $\{H, L^2, L_z\}$. Such an analysis, based on the symmetries of a physical system, is also feasible for the EM cavities.

To further clarify the aspects of degeneracy we briefly consider the example of a 2D empty square cavity of length a, surrounded with metal boundaries. This system has C_{4v} geometrical symmetry. The character table for different point groups are given in the texts by Dresselhaus[57] and by Tinkham.[56] We

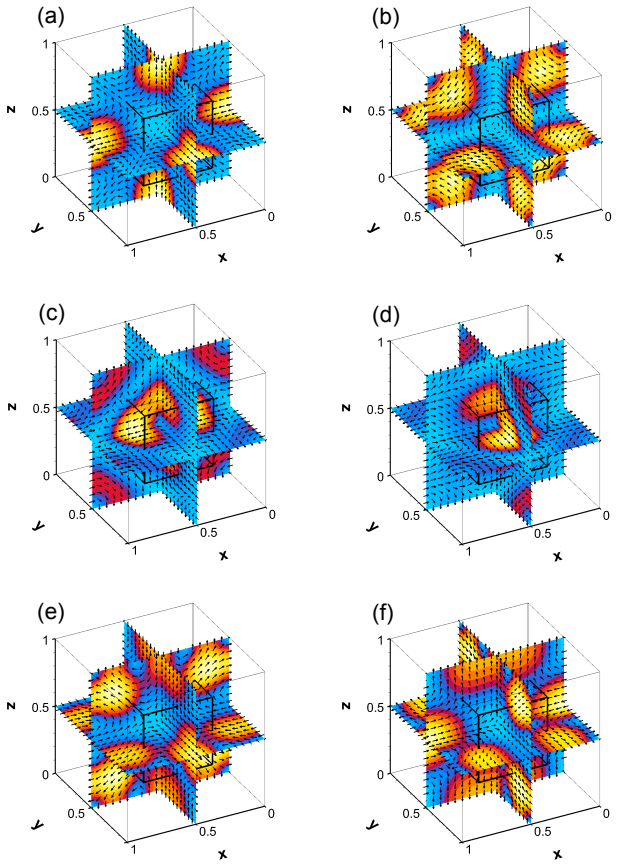

FIG. 16: Electric fields for the symmetry-adapted modes $(1,1,3), (1,3,1), (3,1,1)$, of the dielectrically loaded cavity, with eigenvalues (a) $k_0^2 = 107.43$, (b) $k_0^2 = 107.59$, (c, d) $k_0^2 = 103.73$, and (e, f) $k_0^2 = 107.60$ are shown. The cubic dielectric has dimensions $0.5 \times 0.5 \times 0.5$ mm^3, with a dielectric constant $\varepsilon_2/\varepsilon_1 = 1.2$. The singlets belong to the 1D representations (a) A_{1g}, and (b) A_{2g} of the group O_h. Fields in (c, d) and (e, f) are partners, and each pair form a basis for the 2D representation E. Light yellow (gray) regions correspond to amplitude antinodes, and blue (darker) regions correspond to amplitude nodes. (From Pandey *et al.*, Ref. 38.)

know that the eigenvalues supported in the cavity are given by

$$k_0^2 = \left(n_x^2 + n_y^2\right) \frac{\pi^2}{a^2}, \tag{49}$$

where n_x and n_y are non-zero integers. In Table IX, we list all symmetry-adapted basis functions and irreducible representations for different combinations of (n_x, n_y) modes, derived using Eq. (41). The (odd, odd) or (even, even) doublet with $n_x \neq n_y$ belongs to two distinct irreducible representations. Hence, the degeneracy of these modes is not entirely explained by the symmetry group C_{4v}; therefore they exhibit accidental degeneracy. This is analogous to the situation in an infinite square quantum well, where the accidental degeneracy occurs for the eigenenergies due to the separability of the infinite well potential.[65] Such an accidental degeneracy is rendered normal, in the usual parlance, by recognizing that an

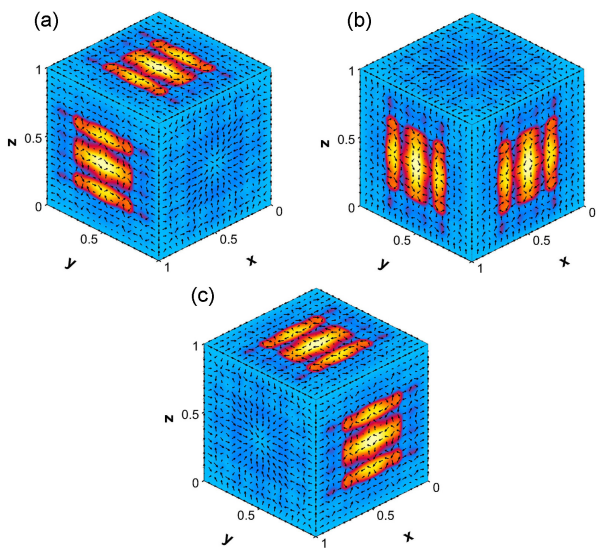

FIG. 17: Surface currents for the symmetry-adapted modes $(0,1,1),(1,0,1),(1,1,0)$, of the dielectrically loaded cavity are shown. The cubic dielectric has dimensions $0.5\times0.5\times0.5$ mm^3, with a dielectric constant $\varepsilon_2/\varepsilon_1=1.2$. Light yellow (gray) regions correspond to amplitude antinodes, and blue (darker) regions correspond to amplitude nodes.

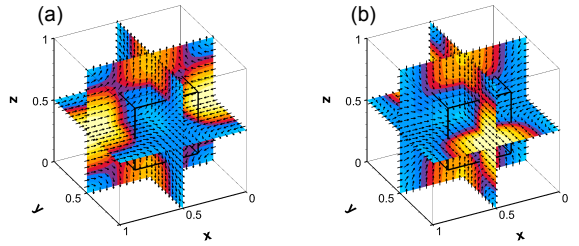

FIG. 18: Degenerate modes $(1,1,1)$ of the loaded cubic cavity are shown. Light yellow (gray) regions correspond to amplitude antinodes, and blue (darker) regions correspond to amplitude nodes. (From Pandey *et al.*, Ref. 38.)

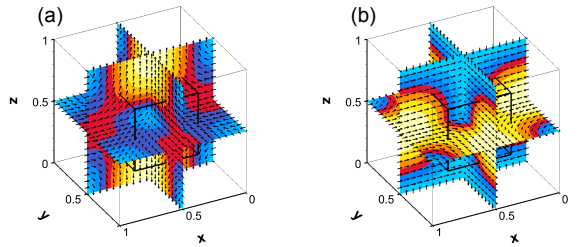

FIG. 19: Non-degenerate modes $(1,1,1)$ of the perturbed loaded cavity belonging to the irreducible representations (a) A_1 with $k_0^2=26.303562$, and (b) B_1 with $k_0^2=26.309544$ are shown. Light yellow (gray) regions correspond to amplitude antinodes, and blue (darker) regions correspond to amplitude nodes. (From Pandey *et al.*, Ref. 38.)

additional operator $\Omega=\left(\partial_x^2-\partial_y^2\right)$ exists, which connects the basis functions of A_1 (A_2) and B_1 (B_2) representations. Hence, the true symmetry of a $2D$ empty square cavity will be a covering group, which is a semidirect product of the geometrical symmetry group C_{4v} and a one-dimensional compact continuous group generated by the operator $\Omega=\left(\partial_x^2-\partial_y^2\right)$.[66] *We can remove the accidental degeneracy in a 2D empty square cavity by introducing a concentric square dielectric inclusion.* Such accidental degeneracy and its removal occurs even in rectangular cavities.

VIII. PHOTONIC CRYSTALS

The first proposals for the design of photonic crystals by Yablonovitch[67] and by John[68] in 1987, and further investigations by Ohtaka, Sakoda, and collaborators[69–73] and by Joannopoulos and Johnson[74] have led to a full appreciation of the physics of periodic dielectrics. With the rapid increases in computing power and simulation techniques and the design and fabrication of PCs, a wide variety of optoelectronic devices including low-loss reflecting surfaces, waveguides, filters, flat lenses, optical inter-connects and the like, have made the efficient prediction of their optical properties a high priority for physicists and optical engineers.[74–79]

By assuming that the PC contains an arbitrarily large number of unit cells, using the Bloch-Floquet Theorem,[80–82] we can decompose the magnetic field into two terms,

$$\mathbf{H}(\mathbf{r})=\mathbf{U}(\mathbf{r})\,e^{i\mathbf{q}\cdot\mathbf{r}}. \tag{50}$$

In the examples treated in this paper, in which the unit cell is a rectangle of dimensions $d_x\times d_y$, the vector $\mathbf{q}$ can be expressed as

$$\mathbf{q}=\frac{\pi q_x}{d_x}\hat{\mathbf{i}}+\frac{\pi q_y}{d_y}\hat{\mathbf{j}}+0\hat{\mathbf{k}}, \tag{51}$$

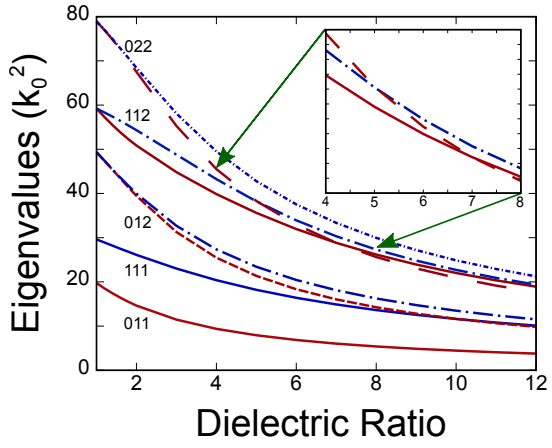

FIG. 20: The evolution of eigenvalues as the dielectric constant in the cavity is varied from 1.0 to 12.0. Sextuplet-level degenerate modes of the empty cavity are seen to split into triplets with the inclusion of cubic dielectric loading. (From Pandey *et al.*, Ref. 38.)

TABLE VIII: We have tabulated the numerically calculated eigenvalues and corresponding Q-factors for a loaded cubic cavity with boundary walls made out of gold. The conducting cavity has dimensions $1\times1\times1$ mm^3; the cubic dielectric loading has dimensions $0.5\times0.5\times0.5$ mm^3, with dielectric ratios $\varepsilon_r=2$ and $\varepsilon_i=10^{-6}$. The conductivity of gold is taken to be $\sigma=4.46\times10^7$ S/m. (From Pandey *et al.*, Ref. 38.)

k_0^2	Q_d -factor	Q_c -factor
14.64474995 $+i$ 0.00000402	3645779.29	78241.13
14.64474995 $+i$ 0.00000402	3645779.29	78241.13
14.64474995 $+i$ 0.00000402	3645779.29	78241.13
26.12581823 $+i$ 0.00000338	7718462.64	62382.25
26.12581823 $+i$ 0.00000338	7718462.64	62382.25
39.45307840 $+i$ 0.00000942	4186986.51	156821.95
39.45307840 $+i$ 0.00000942	4186986.51	156821.95
39.45307840 $+i$ 0.00000942	4186986.51	156821.95
40.02056958 $+i$ 0.00000864	4633182.94	110705.70
40.02056958 $+i$ 0.00000864	4633182.94	110705.70
40.02056958 $+i$ 0.00000864	4633182.94	110705.70
50.87611080 $+i$ 0.00000720	7061660.73	78692.17
50.87611080 $+i$ 0.00000720	7061660.73	78692.17
50.87611080 $+i$ 0.00000720	7061660.73	78692.17
54.34357813 $+i$ 0.00000540	10065812.56	86034.59
54.34357813 $+i$ 0.00000540	10065812.56	86034.59
54.34357813 $+i$ 0.00000540	10065812.56	86034.59
67.50785266 $+i$ 0.00001276	5290879.93	211112.95
67.50785266 $+i$ 0.00001276	5290879.93	211112.95
68.46687536 $+i$ 0.00001114	6146166.21	139534.39
75.30032691 $+i$ 0.00000986	7636781.09	77564.09
75.30032691 $+i$ 0.00000986	7636781.09	77564.09
75.30032691 $+i$ 0.00000986	7636781.09	77564.09

in which the range of q_x and q_y values which comprise the Brillouin zone[83] are $-1<q_x,q_y\leq1$,

It is only necessary to consider the eigenvalues over the first Brillouin zone; outside this zone the eigenvalues will behave periodically. Furthermore, due to reflection symmetries, it is possible to further reduce the Brillouin zone to obtain a greater density of sampling points for the same computational cost. In the first example considered, a square array of cylindrical dielectric posts, the Brillouin zone only needs to be treated over the region marked in Fig. 21.

We can decompose the terms in the functional $\mathbf{L}$ into cell functions and envelope functions. The second term of the integrand of $\mathbf{L}$ reduces to $\mathbf{U}^*\cdot k_0^2\mu_r\cdot\mathbf{U}$. The curl term in the integrand of $\mathbf{L}$ can be simplified using the absence of propagation in the third dimension in Eq. (51) as

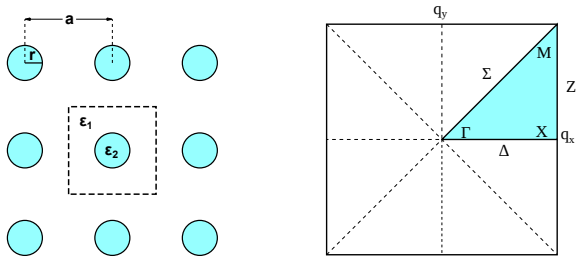

FIG. 21: An array of cylindrical dielectric posts of dielectric constant ε_2 arranged periodically in a medium with a dielectric constant ε_1 is shown. (b) The Brillouin zone for a two-dimensional photonic crystal is shown, where $-1<q_x,q_y\leq1$. The irreducible component of the Brillouin zone has been highlighted. The dashed lines are symmetry lines within the first Brillouin zone.

$$\nabla\times\mathbf{H}= \tag{52}$$
$$e^{i\mathbf{q}\cdot\mathbf{r}}\left[\begin{pmatrix}\partial_yU_z-\partial_zU_y\\ \partial_zU_x-\partial_xU_z\\ \partial_xU_y-\partial_yU_x\end{pmatrix}+i\pi\begin{pmatrix}q_yU_z/d_y\\ -q_xU_z/d_x\\ q_xU_y/d_x-q_yU_x/d_y\end{pmatrix}\right].$$

Eq. (52) may be greatly simplified by classifying all possible solutions into two distinct cases: (*i*) Transverse electric (TE) modes with $E_z=0$, which from the imposition of periodicity resulting in Eq. (52) forces $H_x=H_y=0$, and all other vector components are nonzero and (*ii*) Transverse magnetic (TM) modes with $H_z=0$ which forces $E_x=E_y=0$, $H_z=0$, and all other vector components are nonzero. It is sufficient to consider TE- and TM-modes only, since any fields in the 2D PC can be expressed as a combination of these modes. It is well known that frequencies absent from the eigen spectra of both modes do not propagate because they are in the 'band gap'.

The band gaps of the photonic crystal may be determined by choosing a large number of ordered pairs (q_x,q_y) from within the irreducible Brillouin zone to determine which eigenvalues will propagate. Then the band structure in the remainder of the Brillouin zone may be determined via reflection symmetry. The entire first Brillouin zone may then be translated to adjacent zones due to the periodicity of the cell function.

Given the simple modal decomposition resulting from 2D periodicity, eigenvalue problems for both TE and TM modes can be posed in terms of a single scalar quantity, U_z and its spatial derivatives. For isotropic media where μ_r and ε_r are constant, the functional $\mathbf{L}$ for TM modes simplifies to

$$\mathbf{L}=\int_\Omega d^2r\left[U_z^*\mathbf{A}\cdot\frac{1}{\varepsilon_r}\mathbf{B}U_z-U_z^*k_0^2\mu_rU_z\right], \tag{53}$$

TABLE IX: Different possible even and odd combinations of 2D eigenmodes and their corresponding irreducible representations for the symmetry group C_{4v} are shown. Here the indices n,m are non-zero integers, and the column labeled "irrep" refers to the irreducible representations of the multiplet.

Mode number	"Irrep"	Basis functions
$(2n-1,2n-1)$	B_1	$\mathbf{E}_{(2n-1,2n-1)}$
$(2n,2n)$	A_2	$\mathbf{E}_{(2n,2n)}$
$(2m-1,2n-1)$	B_1	$\mathbf{E}_{(2m-1,2n-1)}+\mathbf{E}_{(2n-1,2m-1)}$
	A_1	$\mathbf{E}_{(2m-1,2n-1)}-\mathbf{E}_{(2n-1,2m-1)}$
$(2m,2n)$	A_2	$\mathbf{E}_{(2m,2n)}+\mathbf{E}_{(2n,2m)}$
	B_2	$\mathbf{E}_{(2m,2n)}-\mathbf{E}_{(2n,2m)}$
$(2m-1,2n)$	E	$\mathbf{E}_{(2m-1,2n)}$, $\mathbf{E}_{(2n,2m-1)}$

where

$$\mathbf{A}=\left[\overleftarrow{\partial_y}-\frac{\pi i q_y}{d_y},-\overleftarrow{\partial_x}+\frac{\pi i q_x}{d_x}\right],\mathbf{B}=\begin{bmatrix}\overrightarrow{\partial_y}+\frac{\pi i q_y}{d_y}\\ \\ -\overrightarrow{\partial_x}-\frac{\pi i q_x}{d_x}\end{bmatrix} \tag{54}$$

and the arrows over the derivatives denote the direction in which the derivatives operate on the quantities in Eq. (53). To obtain $\mathbf{L}$ for TE modes interchange $\varepsilon_r \leftrightarrow \mu_r$ in Eq. (53) and associate U_z with $\mathbf{E}$. Within the FEM, a variational solution is found by the eigenvalue problem derived from $\delta\mathbf{L}=0$ and yields the band structure of the 2D PC.

In the following, we consider three examples of photonic crystals. The first is a square lattice of dielectric posts, for which we obtain the photonic band structure as previously reported in Joannopoulos.[83] We also identify the symmetries at various points in the dispersion relations to discuss band anti-crossing and level degeneracies at special points. The eigenvector fields at the $\Gamma-$point of the frequency dispersion are shown, and frequency bands over the full Brillouin zone are displayed.

The second example is that of a checker-board lattice of dielectric regions. Here again we provide the group theoretic analysis, the band structure, the band surfaces over the Brillouin zone, and the eigenvector fields.

To demonstrate HFEM's capability in modeling systems of arbitrary shapes, the third example is chosen to be a photonic crystal structure based on M. C. Escher's Horsemen tessellation. The fields, band structure and band surfaces over the Brillouin zone are calculated.

A. Group Representation Theory and Photonic Crystals

The eigenvector fields can be organized according to their symmetries with respect to the symmetry group of the crystal and to the group of the wavevector. In the following, we follow the group-theoretic analysis of Sakoda.[69,70,73] The point group of the cylindrical post unit cell is C_{4v}, or the symmetry of the square. The character table of this group is given in Tinkham.[56] The wavevector at the Γ-point has the full symmetry of C_{4v}. The symmetry of the Γ-point modes can be deduced by inspecting the transformation properties of the eigenvectors that are transverse to the extrusion direction of the crystal. For a one-dimensional irreducible representation D_i, operation R_j in class j with character $\chi_i(R_j)$, and eigenvector field v, the eigenvector field will transform according to

$$D_i(R_j)\,v=\chi_i(R_j)\,v. \tag{55}$$

By inspecting the transformation of v by several $D_i(R_j)$, the character table can be used to deduce which irreducible representation the eigenvector field belongs to. As an example, consider the Γ-point mode in Fig. 24a. The transverse vector field satisfies

$$D_i(C_2)v=v,\quad D_i(2C_4)v=v,\quad D_i(2\sigma_v)v=-v. \tag{56}$$

This mode must therefore belong to the irreducible representation with characters

$$\chi_i(C_2)=1,\quad \chi_i(2C_4)=1,\quad \chi_i(2\sigma_v)=-1, \tag{57}$$

which corresponds to the Γ_2 representation. For modes with wavevector away from the Γ-point, the symmetry of the wavevector itself must also be taken into account. The M-point has the full symmetry of C_{4v}. The X-point has the reduced symmetry group C_{2v} (the symmetry of the rectangle) with the character table given in Tinkham.[56] Points along Δ, Z, and Σ have the still further reduced symmetry of C_{1h} (bilateral symmetry) with the character table given in books on group representation theory.[56,57] Points along Z have C_{1h} symmetry due to the fact that a mirror through the line orthogonal

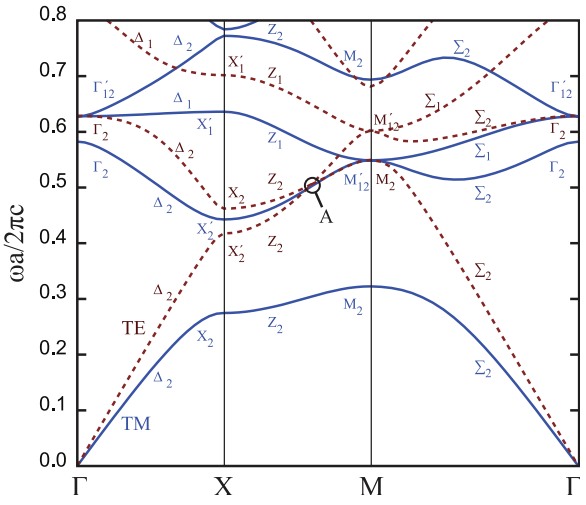

FIG. 22: Eigenvalues for the transverse electric and transverse magnetic modes as calculated using the finite element method with quintic Hermite interpolation polynomials. The point labeled as A is the location of an anticrossing site between the lowest and second-lowest TE modes. This location is shown in higher resolution in Fig. 23.

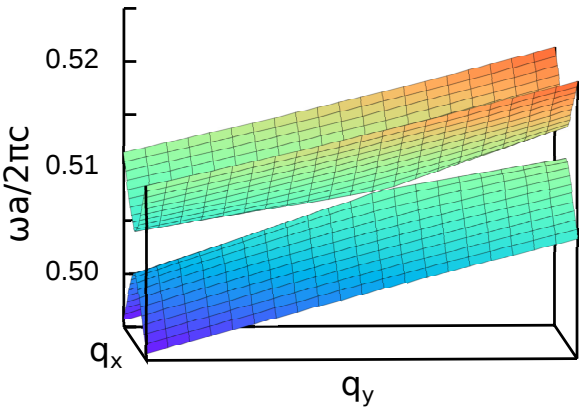

FIG. 23: Close-up view of the anticrossing site shown at point A in Fig. 22. (Adapted from Boucher *et al.*, Ref. 88.)

to the q_x direction brings Z to $Z+Q$, where Q is a reciprocal lattice translation vector.

The dispersion relations for the lowest few modes of the cylindrical post labeled by their irreducible representations are shown in Fig.22. Notice that in Fig. 23 there is an anticrossing site in the TE modes along Z. Since the irreducible representations form an orthogonal basis, anitcrossings can only occur between modes within the same irreducible representation. Indeed, this is the case here, as the two anticrossing modes are in the Z_2 irreducible representation.

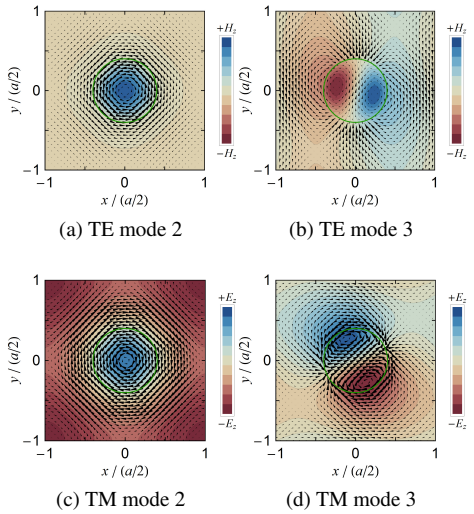

FIG. 24: The electric and magnetic fields of the second and third modes corresponding to the Γ-point in the lattice of cylindrical posts are shown. For TE-modes, the in-plane electric field is represented by vectors and the out-of-plane magnetic field is represented by the gradient background. For TM-modes, the vectors represent the in-plane magnetic field and the background represents the strength of the out-of-plane electric field. Note that the first mode is not shown because the corresponding eigenvalue is zero, resulting in a trivial solution.

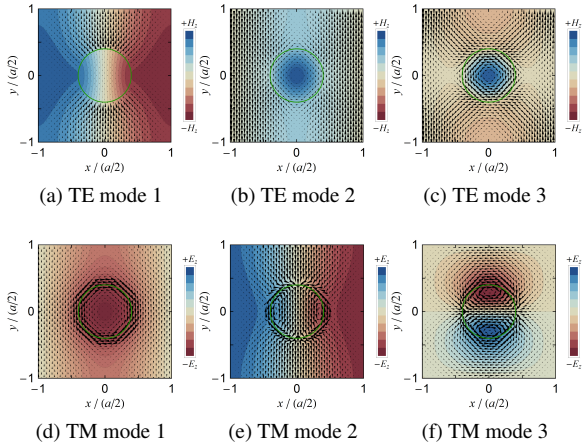

FIG. 25: The electric and magnetic fields of the first three modes corresponding to the X-point in the lattice of cylindrical posts are shown. For TE-modes, the in-plane electric field is represented by vectors and the out-of-plane magnetic field is represented by the gradient background. For TM-modes, the vectors represent the in-plane magnetic field and the background represents the strength of the out-of-plane electric field.

B. Eigenstates for periodic dielectric posts

The band structure for the lattice of dielectric posts was computed using a mesh of 4420 nodes, yielding a matrix size of 26520×26520. The mesh was refined in the region surrounding the edge of the cylindrical post. The curves shown in Fig. 22 give the behavior of the propagating frequencies of radiation at various points along the edge of the irreducible part of the Brillouin zone. The finite element method reproduces a band gap in the TM modes which is also predicted by the planewave method. Using finite elements, it is also possible to increase the resolution close to the anticrossing site marked in Fig. 22. This is a location at which multiple eigenvalues of the same polarization (i.e. both TM or both TE) appear to touch. The close-up view of this point on the edge of the Brillouin zone is given in Fig. 23.

The eigenfunctions for the arrangement of cylindrical dielectric posts are shown in Figs. 24-25. Note that the point symmetries of each mode at the high symmetry points of Γ, X and M can be used, along with their character tables, to verify the symmetry groups shown in Fig. 22 by direct observation of the eigenvector fields.

The dispersion relations are calculated for the irreducible Brillouin zone, which is only one eighth of the full Brillouin zone as shown in Fig. 21, and then their full reconstruction over the entire zone is performed. This can reduce computation time by a factor of 8. The lowest few TE and TM dispersion relations are shown in Figs. 26a-26b. These three-dimensional dispersion surfaces also provide another means of visualizing band gaps in the TE and TM modes, which are of great interest in photonic crystal applications.

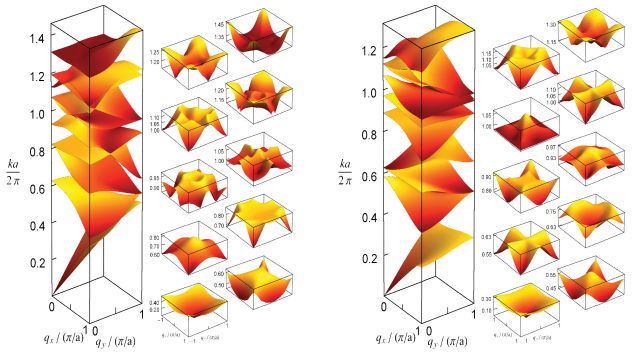

(a) TE mode (b) TM mode

FIG. 26: The eigenvalues of the transverse (a) electric modes and (b) magnetic modes of the periodic lattice of dielectric posts are plotted as surfaces in the first Brillouin zone. On the left side of (a) an (b), the first ten eigenvalues are shown in the irreducible part of the Brillouin zone for TE and TM modes, respectively. On the right side, each eigenvalue has been separated from the rest and extended to the full Brillouin zone through symmetry operations.

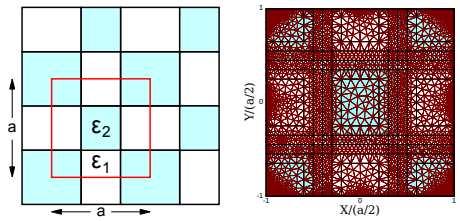

(a) (b)

FIG. 27: (a) A periodic checkerboard pattern with two alternating dielectric materials is shown. Note that the sizes of adjacent checkers within a single unit cell do not necessarily match. (b) A sample finite element mesh is given for the unit cell of a checkerboard lattice. Mesh refinement occurs at all of the checker boundaries.

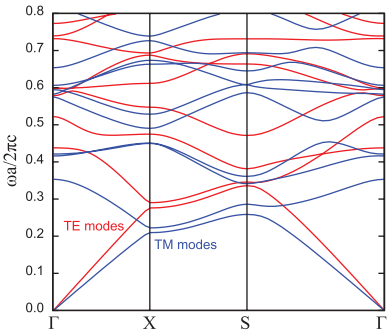

FIG. 28: Eigenvalues for the transverse electric and transverse magnetic modes for the checkerboard arrangement.

C. Eigenstates for a checkerboard lattice

We present results for a checkerboard superlattice of dielectric posts which is readily solved using HFEM. The band structure for a checkerboard lattice was computed using a mesh of 12355 nodes, yielding a matrix size of 74130×74130. The mesh was refined in the region surrounding the edges within the checkerboard. Since the checkerboard lattice has more internal boundaries per unit cell than the cylindrical post geometry, a greater degree of mesh refinement was required, resulting in a larger global matrix than that of the lattice of cylindrical posts.

The eigenvalues are plotted over a triangular path between the Γ, X and S points. Compared to the dielectric posts, the checkerboard shows much more activity and a denser band structure at low frequencies, but it has a smaller band gap in the TM modes. Like the cylindrical posts, this checkerboard has no TE band gap. The corresponding eigenfunctions for the lowest modes at the high-symmetry points are plotted in Figs. 29a-29d.

The vectors represent the electric field in TE modes and the magnetic field in TM modes, while the shading of the

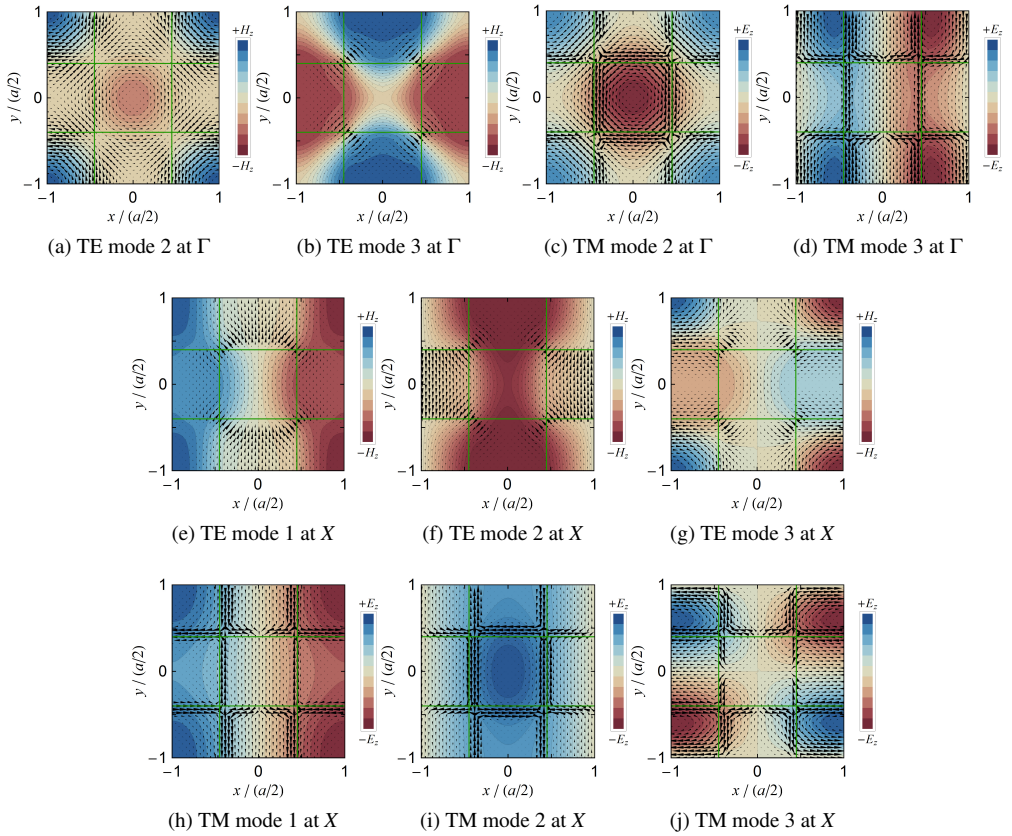

FIG. 29: The electric and magnetic fields of the second and third modes corresponding to the Γ-point in the checkerboard lattice are shown from (a) to (d), while the fields of the first three modes corresponding to the X-point are shown from (e) to (j). For TE-modes, the in-plane electric field is represented by vectors and the out-of-plane magnetic field is represented by the gradient background. For TM-modes, the vectors represent the in-plane magnetic field and the background represents the strength of the out-of-plane electric field. Note that the first mode is not shown because the corresponding eigenvalue is zero, resulting in a trivial solution.

background represents the intensity of the magnetic field in TE modes and the electric field in TM modes, with lighter shades corresponding to regions of greater field magnitude. Note that the eigenfunction for the lowest eigenvalue is omitted for the Γ-point for both modes of propagation. This is because those lowest eigenvalues approach zero at the Γ-point, causing the corresponding eigenfunctions to be trivial (zero everywhere).

The dispersion relations calculated for the irreducible Brillouin zone and then their full reconstruction over the entire zone is performed. The lowest few TE and TM dispersions are shown in Figs. 30a-30b.

D. Eigenstates for an Escher tessellation

In order to demonstrate the flexibility of the Finite Element Method, a photonic crystal based on a tessellation by M. C. Escher was simulated and its band structure was calculated. The image used to produce the crystal was Escher's "Horsemen" as shown in Fig. (31a). A sample mesh is given in Fig. (31b).

The band structure for the Escher tessellation was computed using a mesh of 54945 nodes, yielding a matrix size of 329670×329670. Since the Escher unit cell does not have the same reflection symmetries as cylindrical and checkerboard unit cells, the entire Brillouin zone was tested instead of a small fraction of it.

The eigenvalues are plotted over a triangular path between the Γ, X and S points in Fig. (31c). The transverse electric modes appear to converge to a band structure similar to that of the cylindrical post, even featuring an anticrossing site in approximately the same position. However, the transverse magnetic modes fail to converge properly, even when using several tens of thousands of nodes. This may be due to the high complexity of the dielectric structure coupled with the slow error convergence of the action formulation based on **D**. The corresponding eigenfunctions for the lowest modes at the high-symmetry points are plotted in Figs. 32a-32d.

The vectors represent the electric field in TE modes and the magnetic field in TM modes, while the shading of the background represents the intensity of the magnetic field in TE modes and the electric field in TM modes. As with the other crystal geometries, we omit the lowest state at the Γ-point as a trivial solution.

The eigenvalues have also been plotted as surfaces over the first Brillouin zone, as shown in Figs. 33a and 33b.

In conclusion, we anticipate that the use of Hermite FEM will allow the treatment of multiscale problems associated with photonic crystals with embedded quantum dots, defects, and the like. The spatial representation of the fields using Hermite triangular interpolation is much more economical than employing plane-wave methods for such structures allowing the deployment of more finite elements strategically in specific regions as needed. The resulting global matrices are still sparse and banded due to the local connectivity, which leads to far more compact matrices than in other schemes with the concomitant reduction in compute-time. While the transverse magnetic modes continue to converge slowly in complex geometries, the efficient calculation of the TE modes allows one to easily determine which geometries have TE band gaps. Furthermore, the extension to three-dimensional crystals, in which a separate formulation based on **D** is no longer needed, may alleviate this problem.

IX. CONCLUDING REMARKS

Electromagnetic devices of higher frequencies (e.g., mm-wave) and increasing complexity are being employed in a wide variety of industries. The design of modern electronic includes electromagnetic components with sophisticated interactions both in isolation and in integrated combinations. Designing these components requires a significant amount of modeling and simulation and these demands continue to increase with higher levels of integration. At the nanoscale, similar circumstances are faced for optical interconnects, quantum well laser design, and in plasmonics. Again, reliable simulations are essential to ensure that each device does not affect

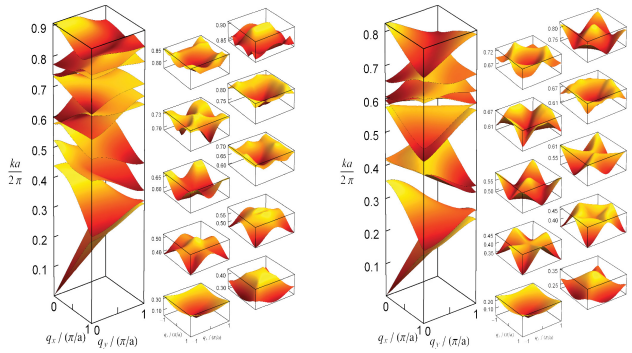

(a) TE mode (b) TM mode

FIG. 30: The eigenvalues of the transverse (a) electric modes and (b) magnetic modes of the checkerboard lattice of dielectric posts are plotted as surfaces in the first Brillouin zone. On the left side of (a) an (b), the first ten eigenvalues are shown in the irreducible part of the Brillouin zone for TE and TM modes, respectively. On the right side, each eigenvalue has been separated from the rest and extended to the full Brillouin zone through symmetry operations.

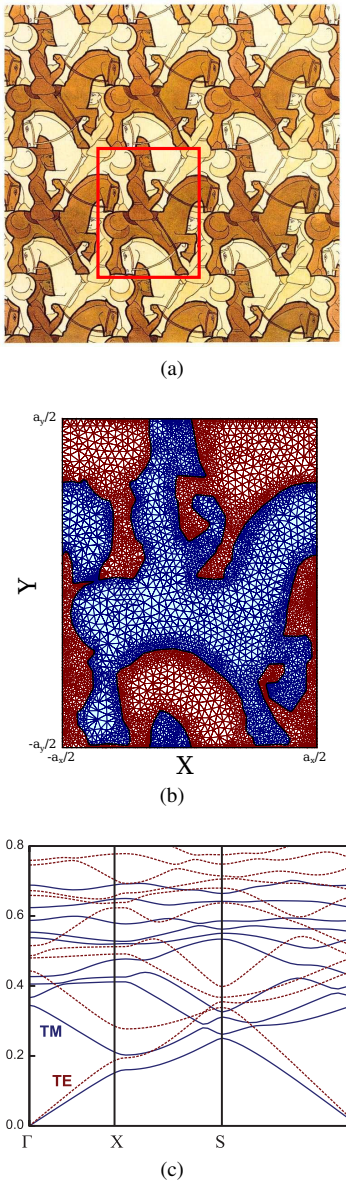

(a) (b) (c)

FIG. 31: (a) The unit cell of a PC based on "The Horsemen" by M. C. Escher is shown. The Escher tessellation was chosen to illustrate the capacity of the HFEM to calculate the band structures of complicated geometries with unique symmetry properties.[84] (b) A sample mesh is given for the unit cell of an Escher tessellation. The regions are assigned ε_r =8.9, 1.0 to form a 2D PC. Most calculations used more refined meshes than shown in (b), including 54,945 nodes for a total of 329,670 global degrees of freedom. (c) TE (dashed) and TM (solid) eigenmodes for the associated 2D PC are shown. (Adapted from Boucher *et al.*, Ref. 88.)

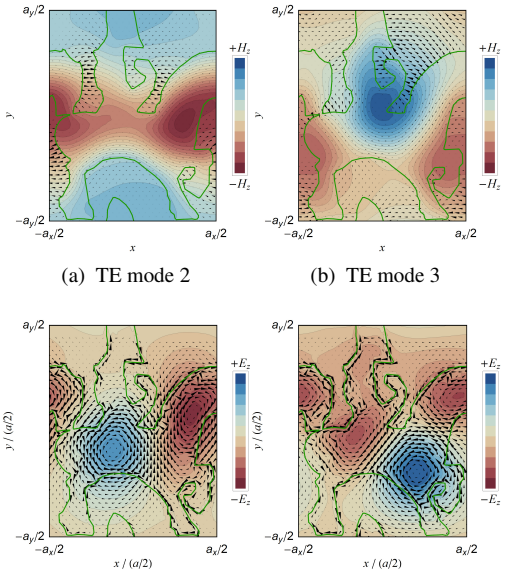

(a) TE mode 2 (b) TE mode 3

(c) TM mode 2 (d) TM mode 3

FIG. 32: The **E** and **H** fields of the second and third modes at Γ for the Escher lattice are shown. For (a,b), $E_{x,y}$ are represented by vectors and H_z by the contours. For (c,d), $H_{x,y}$ are represented by vectors and E_z by the contours. (Adapted from Boucher *et al.*, Ref. 88.)

others near it through electromagnetic cross-talk. The novel effects exhibited by metamaterials containing negative refractive index components are all simulated before being assembled in order to optimize their optical properties as desired.

Commercial computational electromagnetic modeling software relies heavily on vector finite element, finite difference, and spectral methodologies. Here we focus on a scalar finite element approach in which the field components are approximated using local polynomials over discrete subdomains. We show that the use of Hermite interpolation polynomials provide very accurate solutions with a minimal number of elements used in the discretization. The ability to reproduce smooth variational solutions for the fields will allow a coarsely discretized full-wave maxwell solver to seamlessly couple to other solvers for physically small features, such as small gate geometries, quantum wells and dots, or plasmonic structures which are all deeply subwavelength. The Hermite interpolation polynomials are equally well suited to three-dimensional finite elements, e.g., 40 DOF or 56 DOF can be used to define the basis functions on tetrahedra.

We have shown that the hermite interpolation polynomials on a triangular element are able to eliminate the spurious solutions that typically occur with Lagrange-type scalar shape functions. The results for the standard rectangular waveguide with and without a dielectric inhomogeneity directly demonstrate the efficacy of this method. The eigenfrequency for the lowest mode for the homogeneous waveguide agrees with the analytical result within a relative error of 10^{-15}, which is superior to hierarchical VFEM for about the same number of DOF.[28]

For the inhomogeneous waveguide, we have calculated the eigenmodes that are trigonometric in both regions at higher frequencies, and they evolve into solutions that are sinusoidal in the higher dielectric region and hyperbolic in the region with the lower dielectric as the dielectric ratio $\varepsilon_2/\varepsilon_1$ increases. This behavior is analogous to the development of above-barrier states in quantum wells that get localized and captured into the quantum well as the well depth is increased. This analogy suggests that as ε_2 is increased more modes are captured by the higher dielectric region leading to the sinusoidal behavior in the larger dielectric region and an exponential decay into the lower dielectric region.

For cubic cavities, we have shown that electromagnetic simulations done with Hermite elements deliver high accuracy and smoother representation of fields. We have compared our formalism with analytical results. Fewer finite elements are needed to achieve comparable results for eigenvalue calculations.

The divergence-free constraint for the electromagnetic

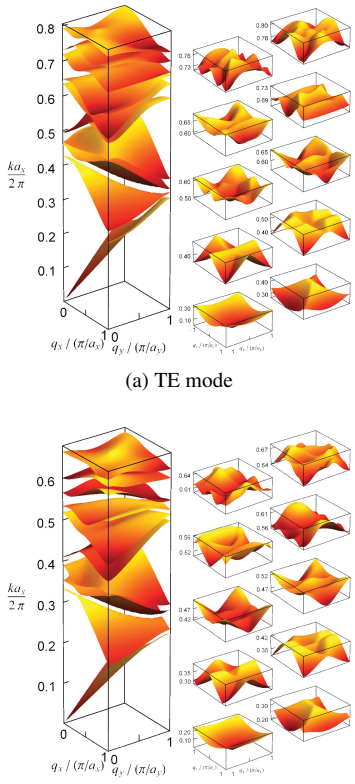

(a) TE mode

(b) TM mode

FIG. 33: The eigenvalues of the transverse (a) electric modes and (b) magnetic modes of the Escher superlattice of dielectric posts are plotted as surfaces in the first Brillouin zone. On the left side of (a) an (b), the first ten eigenvalues are shown in the irreducible part of the Brillouin zone for TE and TM modes, respectively. On the right side, each eigenvalue has been separated from the rest and extended to the full Brillouin zone through symmetry operations.

TABLE X: We present here a summary, and contrast the properties between VFEM and HFEM calculations.

VFEM	HFEM
• In 2D, there are no spurious solutions with edge-elements. • Field directions are ill-defined at all the nodes. With increasing mesh density we have more area (2D) and volume (3D) around nodes where the field direction is not defined. Thus mesh refinement does not give improved results in applications. • In 3D, all zero-frequency solutions are pushed to the null-space through Nedelec compliant shape functions. Estimates are that for a matrix dimensions of 10^3 in typical EM calculations, there are about 20%–30% solutions to the matrix that are in this category.[9] They have to be calculated and then thrown away, being unusable solutions. Carrying this overhead in the calculation is computationally expensive when considering sophisticated structures.	• In 2D, there are no spurious solutions using Hermite finite elements with triangles.[22,33] • This is a node-based FEM, and there are no issues with field directions at nodes and throughout, including for 3D hexahedral Hermite elements. Mesh refinement allows the improved identification of spurious solutions in the positive spectrum. • In 3D, a modest penalty factor $\lambda = 1$ pushes spurious solutions to the zero-frequency sector and they do not appear in the calculated range of the spectrum. Some are left over, and these affect the non-zero frequency spectrum. Now the node-based divergence condition is super-imposed on the penalty calculation; this leads to substantial improvement in the separation and identification of the spurious solutions. The key is the tag provided by $\|\nabla\cdot\mathbf{E}\|/\|\nabla\times\mathbf{E}\|$. This ratio keeps increasing for the spurious solutions, whereas it decreases substantially for physically admissible solutions as the mesh is refined.
• The multi-scale modeling for multi-physics systems cannot be performed: for example, modeling a vertical cavity surface emitting laser.	• Being node based, the modeling can accommodate multi-scale problems for multi-physics applications.

fields results in spurious solutions for the wave equation. Their eigenfrequencies are pushed to zero in the VFEM, either through Nedelec compliance or through their removal at each iteration. In either case, this is an expensive numerical procedure. In our approach, we imposed the divergence-free condition by adding a constant penalty term (a Lagrange multiplier, set to unity). In addition, through the derivative degrees of freedom at each node we have imposed the same constraint explicitly. Now the remaining few non-zero frequency spurious solutions are eliminated by identifying them through their large $|\nabla\cdot\mathbf{E}|/|\nabla\times\mathbf{E}|$ ratio. This procedure does not alter or influence the accuracy of the physical solutions. Comparison of properties between VFEM and HFEM calculations are presented in Table X.

Group theoretical classification of eigenmodes in photonic crystals,[69,70] in radio-frequency cavities,[85,86] and in metamaterials[87] were previously discussed in the literature. We have considered the symmetries of a metallic cubic cavity, with and without a dielectric inclusion. The origin of higher degeneracy in the frequency spectrum in a cubic cavity are attributed to the existence of accidental degeneracy. The operators additional to those of the symmetry group O_h have been determined. We have derived a coefficient formula[34] which will classify, and project out the symmetry adapted modes of the corresponding irreducible representation. The computed field distributions are symmetry-adapted as predicted from group theory.

The accidental degeneracy is lifted with the insertion of a concentric cubic dielectric of a smaller size. The variation of the spectrum as the ratio $\varepsilon_2/\varepsilon_1$ is changed has been explored. We have shown that this leads to a reordering of some of the mode frequencies.

Since the FEM is based on geometry discretization, we are now free to change the shape of the cavity and still obtain a high accuracy using HFEM. This method is well suited for mixed-physics applications, such as for quantum well lasers in electromagnetic cavities. This is because we have node-based finite elements with scalar shape functions.

Applications to multiscale analysis is now feasible using the present method. This option is not open to VFEM due to the lack of directionality for fields at shared nodes in the finite element mesh. Very dense meshes lead to larger regions in which field directions are ill-defined. Typically, quantum mechanical problems are solved with scalar basis functions, and the electromagnetic problems are dealt separately with VFEM or other techniques. HFEM formulation facilitates an identical scheme for solving simultaneously both electromagnetic and quantum mechanical/acoustic calculations.

We have shown that the scalar Hermite polynomials have several fundamental advantages for obtaining the band structure of periodic systems such as photonic crystals, while compared with VFEM and other plane wave expansion methods.[88] Advantages are observed in computational costs, the ability to capture spatial complexity in the dielectric distributions, a substantially higher numerical convergence with scaling, and in obtaining variational eigenfunctions free of numerical artifacts. We note that the method delineated in this paper is well suited to model and design composite structures such as

3D photonic band-gap crystals, metamaterials and topological photonic systems, for applications in ultra-small optical integrated circuits. Hence, approaches reviewed here show great promise for the simulation of electrodyamics, plasmonics, high frequency circuitry, and especially in mixed physics problems.

Finally, we note that the importance of accidental degeneracy and its consideration is because the periodic table of elements and its structure depend on it. The progression of elements in the table with the addition of more and more electrons to the atoms is governed by the Pauli exclusion principle and his "aufbau prinzip." This then governs all of chemistry and hence all of biology. May we be permitted to say that life itself depends on accidental degeneracy?

Given the periodic nature of the PCs, it is natural that the vast majority of published works on photonic band structure calculations are analogous to the reciprocal space analysis common to the solid state physics analysis of propagating electronic states in crystals. The analogy to solid-state has some drawbacks. In particular the abrupt, macroscopic discontinuities of dielectric regions make it difficult to transform the dielectric function and EM states between reciprocal space and real space without artifacts. In practical use, these numerical artifacs can become sources of serious error when subsequent calculations in real space are required or the system symmetry is lowered. Interactions with sub-wavelength features, such as quatum structures that are most often at interfaces, can be very difficult to resolve if the EM field description is coarse. Other demanding examples are the computation of localized states (such as defects) and slab geometries.[89] Under conditions of a periodic slab, the predominant approach is to move away from the use of 10^6 plane waves (the 2D periodic system of a slab), plane waves corresponding to the third dimension, plus supercells corresponding to any irregularity[90,91] toward the time domain where finite-difference time-domain calculations are now widely used for the calculation of real-space EM fields.

VFEM calculations for the eigenmodes of PCs and VFEM-time-domain calculations for waveguide and defect geometries are not common, but examples include the real-space construction of localized Wannier basis function from the perfect crystal eigenmodes to compute localized defect modes.[92] One disadvantage of such calculations is the pixelization of the resulting fields owing to the lower order of normal field continuity in vector element formalism or the spatial gridding of finite-difference time domain analysis. This mixed order real space description results in an EM field that is spatially coarser than the quantum mechanical features of embedded solid state structures such as quantum dots, wells, and other features common to modern semiconductor devices.

It is ultimately more desirable to obtain field patterns that have continuous spatial derivatives within dielectric layers for convenient calculation of quantum mechanical or deeply sub-wavelength interactions. The present HFEM approach provides smoothly varying EM wavefunctions using a nodal mesh description and derivative continuity, yet preserves the necessary boundary conditions and numerical constraints that have been demanded of VFEM. Accurate spatial field description provided by HFEM will be important in inverse design schemes for PCs to engineer the topology of band structures.[93,94]

For decades, PC analysis by reciprocal space techniques has produced accurate eignevalue results as would be expected of a variational approach, however the HFEM offers a flexible, robust means of computing the eigenstates of a PC with much more physical eigenfunctions at far lower computational cost. In our calculations, we note that the typical matrix dimensions for the PC with square geometry containing cylindrical posts are on the order of 26×10^3; however, the local connectivity within HFEM leads to a banded matrix with 0.158% occupancy. This sparsity is a demonstrable advantage over the plane-wave method. The ability to construct the field distributions from the nodal eigenvectors with no discontinuities in the reconstructed function and its derivatives is an additional benefit and allows for a high quality description of the dual fields. Furthermore, the plane-waves are global functions, and the eigenfunctions constructed using these functions have the usual errors on the order of the square root of the errors in the eigenvalues. However, in FEM, this error can be distributed nonuniformly by emphasizing areas (or volumes) of interest through the redistribution of elements, putting more elements in those areas that are of particular interest and fewer elsewhere. The detailed agreement with the published results for the square lattice of dielectric posts shows that the HFEM provides accurate, reliable results that are derivable with banded, sparse matrices.

The ability of the FEM to represent complex geometries is highlighted by considering the use of an Escher tessellation to define a unit cell of a PC. The same example treated with reciprocal space methods would require an enormous number of Fourier components to capture the details of the geometry.

For HFEM to be fully extensible across a wider range of PC modeling, it will be necessary to demonstrate its applicability in three dimensions. This is straightforward with Hermite tetrahedral and brick elements. As a node based method, HFEM is suited for domain decomposition and can be connected with existing frameworks for treating the open domains of finite systems as well. A final feature that would be required in this context is the exploration of the time-domain evolution of solutions. The finite element time-domain techniques that are already prevalent in modeling such structures can readily incorporated with the methods we have reviewed in this paper.

In conclusion, we can anticipate that the use of HFEM will allow the treatment of multiscale and multi-physics problems that require detailed spatial descriptions of EM fields. With the solutions given on the vertices of the triangle and the continuity guaranteed both for the normal and tangential derivatives at triangle interfaces, it becomes substantially simpler to mix scalar-vector field calculations involving curl operators. This a distinct advantage over reciprocal space methods as we have shown through cases designed to stress the sophistication of the spatial reconstruction of fields.

X. ACKNOWLEDGMENTS

We thank J. D. Albrecht, C. R. Boucher, and S. Pandey for valuable discussions. DNP thanks Worcester Polytechnic Institute for summer undergraduate research fellowships. Computational resources for the calculations presented in this article are provided by the Center for Computational NanoScience at WPI.

[1] A. Sommerfeld, Ann. der Phys. Chem. **67**, 233–290 (1899).
[2] J. S. Schwinger and David S. Saxon, *Discontinuities in Waveguides: Notes on Lectures by Julian Schwinger* (Taylor & Francis US, January 1968).
[3] K. A. Milton and J. Schwinger, *Electromagnetic Radiation: Variational Methods, Waveguides and Accelerators* (Springer, Berlin, Germany, 2006).
[4] K. Leong, W. R. Deal, V. Radisic, M. X. Bing, J. Uyeda, L. Samoska, A. Fung, T. Gaier, and R. Lai, IEEE Microwave and Wireless Components Letters **19**, 413–415 (2009).
[5] J. C. Nedelec, *Mixed finite elements in R3*, Numerische Mathematik, vo1.35, pp. 315–341 (1980).
[6] D. Sun, J. Manges, X. Yuan, and Z. Cendes, IEEE Antennas and Propagation **37**, 12–24 (1995).
[7] D. R. Lynch and K. D. Paulsen, IEEE Trans. Microwave Theory Tech., vol **39**, pp 395–403 (1991).
[8] J. F. Lee, D. K. Sun and Z. J. Cendes, IEEE Transactions on Magnetics **27**, pp. 4032–4035 (1991).
[9] A. F. Peterson, IEEE Transactions on Antennas and Propagation, vol.**43**, pp. 357–365 (1994).
[10] J. P. Webb, Rep. Prog. Phys. **58**, 1673–1712, (1995); also see, IEEE Trans. on Magn.**24**, 162–165 (1988).
[11] L. S. Anderson and J. L. Volakis, IEEE Transactions on Antennas and Propagation 47, 112 (1999).
[12] J. P. Webb, IEEE Transactions on Antennas and Propagation 47, 1244 (1999).
[13] D. Boffi, P. Fernandes, L. Gastaldi, and I. Perugia, SIAM Journal of Numerical Analysis 36, 1264 (1999).
[14] J. P. Webb, IEEE Transactions on Magnetics 37, 3600 (2001).
[15] H. X. Zheng, L. Y. Feng, and Q. S. Wu, IEEE Transactions on Microwave Theory and Techniques 58, 128 (2010).
[16] O. Tuncer, Chuan Lu, N.V. Nair, B. Shanker, L.C. Kempel, IEEE Trans. Ant. Prop. **58**, 887 (2010).
[17] Z. Li and L. R. Ram-Mohan, Phys. Rev. E **85**, 016706 (2012).
[18] L. Xuan, B. Shanker, Z. Zeng, and L. Udpa, Int. J. Applied Electromagnetics and Mechanics **19**, 463 (2004).
[19] J. Sladek, V. Sladek, and E. Pan, Int. J. Solids Struct. **50**, 3975 (2013).
[20] G. R. Liu and Y. T. Gu, *An Introduction to Meshfree Methods and Their Programming*, (Springer, Dorderecht, 2005).
[21] J. P. Webb, IEEE Transactions on Magnetics **24**, 162–165 (1988).
[22] For details on the Hermite polynomials on a triagular element, see P. G. Kassebaum, C. R. Boucher, L. R. Ram-Mohan, J. Comp. Phys. **231**, 5747 (2012).
[23] K. Bell, International Journal for Numerical Methods in Engineering, **1**, 101–122 (1969).
[24] I. Holand and K. Bell, *Finite Element Methods in Stress Analysis* (Tapir, Trondheim, 1970).
[25] J. H. Argyris, I. Fried, D. W. Scharpf, Imperial College of Science and Technology, University of London, Technical Note 14, 701–709 (1968).
[26] Gouri Dhatt and Gilbert Touzot, *The Finite Element Method Displayed*, (John Wiley & Sons, April 1984)
[27] L. R. Ram-Mohan, *Finite Element and Boundary Element Applications in Quantum Mechanics* (Oxford, New York, 2002).
[28] S. C. Lee, J. F. Lee, and R. Lee, IEEE Transactions on Microwave Theory and Techniques 51, 1897 (2003).
[29] K. Hayata, M. Koshiba, M. Eguchi, and M. Suzuki, IEEE Trans. Microw. Theory Tech. **MTT-34** 1120–1124 (1986).
[30] Z. J. Cendes and P . Silvester, IEEE Trans. Microw. Theory Tech. **MTT-18**, 1124-1131 (1971).
[31] S. Ahmed and P. Daly, IEE Proceedings, **116**, 1661–1664 (1969).
[32] Jianming Jin, *The Finite Element Method in Electromagnetics*, 2nd ed. (Wiley, New York, 2002).
[33] C. R. Boucher, Z. Li, C. I. Ahheng, J. D. Albrecht, L. R. Ram-Mohan, Journal of Applied Physics 119 (14), 143106 (2016).
[34] Sathwik Bharadwaj, Siddhant Pandey, and L. R. Ram-Mohan, Phys. Rev. B **96**, 195305–1–13 (2017).
[35] COMSOL Multiphysics®, version 5.2. https://www.comsol.com, COMSOL AB, Stockholm, Sweden.
[36] Ansoft. ANSYS HFSS®, 3D full-wave electromagnetic field simulation; https://www.ansys.com/products/electronics/ansys-hfss.
[37] MFEM: Modular Finite Element Methods Library, doi: 10.11578/dc.20171025.1248.
[38] Siddhant Pandey, Sathwik Bharadwaj, M. Santia, M. Hodek, J. D. Albrecht and L. R. Ram-Mohan, J. Appl. Phys. **124**, 213106 (2018).
[39] B. M. A. Rahman, J. B. Davies, IEEE Trans. Microw. Theory Tech. **MTT-32**, 20–28 (1984).
[40] J. P. Webb, IEEE Trans. Microw. Theory Tech. **MTT-33**, 635–639 (1985).
[41] A. Konrad, IEEE Trans. Magn. **25**, 2822–2824 (1989).
[42] C. M. Pinciuc, A. Konrad, and J. D. Lavers, IEEE Trans. Magn. **50**, 7200113 (2014).
[43] C. M. Pinciuc, Doctoral dissertation, University of Toronto (2012).
[44] M. H. Nayfeh, M. K. Brussel, (John Wiley & Sons, New York, 1995); Ch. 16, 549–552.
[45] A. M. Portis, *Electromagnetic Fields: Sources and Media* (John Wiley, New York, 1978); pp508–513.
[46] R. F. Harrington, *Time-Harmonic Electromagnetic Fields* (John Wiley and Sons, New York, 2001).
[47] J. D. Jackson, *Classical Electrodynamics*, 3rd Ed. (Wiley, New York, 1999).
[48] D. J. Griffiths, *Introduction to Electrodynamics*, 4th Ed. (Pearson Education, 2013).
[49] S. H. Wong and Z. J. Cendes, IEEE Trans. Magn. **24**, 2685–2687 (1988).
[50] Gerrit Mur, IEEE Trans. Magn. **30**, 3552–3557 (1994).
[51] P. Arbenz and R. Geus, Appl. Numer. Math. **54**, 107–121 (2005).
[52] A. Dziekonski, M. Rewienski, P. Sypek, A. Lamecki and M. Mrozowski Commun. Comput. Phys. **22**, 997–1014 (2017).
[53] V. Hernandez, J. E. Roman, and V. Vidal, ACM Trans. Math. Software, **31**, 3, 351–362 (2005).
[54] Satish Balay *et al.*, Argonne National Laboratory, ANL-95/11 - Revision 3.7, 2016. *PETSc Users Manual.*
[55] P. R. Amestoy, I. S. Duff, J.-Y. L'Excellent, and J. Koster, SIAM J. Matrix Anal. Appl. **23**, 15–41 (2006).
[56] M. Tinkham, *Group Theory and Quantum Mechanics* (Dover Publications, New York, 2003).
[57] M. S. Dresselhaus, G. Dresselhaus and A. Jorio, *Group Theory: Application to the Physics of Condensed Matter* (Springer, Berlin, 2008).
[58] F. M. Fernandez, arXiv:1310.5136.
[59] D. S. Jones, *The Theory of Electromagnetism* (The Macmillan Company, New York, 1964).
[60] D. F. Greenberg, Am. J. Phys. **34**, 1101–1109 (1966).
[61] V. Fock, Z. Phys. **98**, 145–154 (1935).
[62] W. Pauli, Z. Physik **36**, 336–363 (1926).
[63] C. E. Burkhardt and J. J. Leventhal, Am. J. Phys. **72**, 1013–1016 (2004).
[64] H. V. McIntosh, *Symmetry and degeneracy*, in *Group Theory and Its Applications*, p. 75-144, edited by E. M. Loebl (Academic Press, NY, 1971).
[65] J. Shertzer and L. R. Ram-Mohan, Phys. Rev. B **41**, 9994–9999 (1990).
[66] F. Leyvarz, A. Frank, R. Lemus and M. V. Andrez, Am. J. Phys. **65**, 1087–1094 (1997).
[67] E. Yablonovitch, Phys. Rev. Lett. **58**, 2059–2062 (1987).
[68] S. John, Phys. Rev. Lett. **58**, 2486 (1987).
[69] K. Sakoda, Phys. Rev. B **52**, 7982 (1995).
[70] K. Sakoda, Phys. Rev. B **55**, 15345 (1997).
[71] K. Ohtaka and M. Inoue, Phys. Rev. B **19**, 5057 (1979).
[72] K. Ohtaka, Y. Tanabe, Journal of the Physical Society Japan **65**, 2670–2684 (1996).
[73] K. Sakoda, Optical Properties of Photonic Crystals (Springer, Berlin, Germany, 2001).
[74] S. G. Johnson, J. D. Joannopoulos, *Photonic Crystals: The Road from Theory to Practice* (Kluwer, Massachusetts, 2002), and references therein.
[75] J. B. Pendry, J. Mod. Opt. **41**, 209 (1994).
[76] J. B. Pendry, Phys. Rev. Lett. **85** 3966 (2000).
[77] D. R. Smith, Willie J. Padilla, D. C. Vier, S. C. Nemat-Nasser and S. Schultz, Phys. Rev. Lett. **84**, 4184 (2000).

[78]H. Benisty, V. Berger, J.-M Gérard, D. Maystre, A. Tchelnokov, *Photonic Crystals: Towards Nanoscale Photonic Devices* (Springer, Berlin, Germany, 2005).
[79]V. G. Veselago, Soviet Phys. Usp. 10, 509–514 (1968) [Usp. Fiz. Nauk 92, 517–526 (1967).
[80]C. Kittel, *Introduction to Solid State Physics* (John Wiley & Sons, New York, 2005).
[81]F. Bloch, Zietshrift der Physik **52**, 555-600 (1928).
[82]G. Floquet, Annales de l'École Normale Supérieure **12** 47-88 (1883).
[83]J. D. Joannopoulos, S. G. Johnson, J. N. Winn, R. D. Meade, (Princeton, New Jersey, 2008), p. 66-71. (The solid curves in Fig. 1(a) are reproduced with permission from Princeton University Press.)
[84]Fig. 4(a) has been used by permission, www.mcescher.com. Copyrights for all M.C. Escher works©2010 are with the M.C. Escher Company - the Netherlands. All rights reserved.
[85]S. Sakanaka, Phys. Rev. ST Accel. Beams **8**, 072002 (2005).
[86]P. R. McIsaac, IEEE Trans. Microw. Theory Tech. **MTT-23**, 421–433 (1975).
[87]W. J. Padilla, Optics Express **15**, 1639–1646 (2007).
[88]C. R. Boucher, Zehao Li, J. D. Albrecht, and L. R. Ram-Mohan, J. Appl. Phys. **115**, 154101–1–10 (2014).
[89]B. Jiang, W. Zhou, W. Chen, A. Liu, and W. Zheng, J. Appl. Phys. **111**, 053103 (2012).
[90]S. Fan and J. D. Joannopoulos, Phys. Rev. B **65**, 235112 (2002).
[91]S. G. Johnson, S. Fan, P. R. Villeneuve, J. D. Joannopoulos, and L. A. Kolodziejski, Phys. Rev. B **60**, 5751 (1999).
[92]P. Sotirelis and J. D. Albrecht, Phys. Rev. B **76**, 075123 (2007).
[93]W. Li, F. Chen, Y. Chen, Y.F. Li and X. Huang, Adv. Theory Simul. **2**, 1900017 (2019).
[94]Z. Lin, L. Christakis, Y. Li, E. Mazur, A. W. Rodriguez, and M. Lončar, Phys. Rev. B **97**, 081408(R) (2018).